Egypt. J. Chem. **Vol. 66**, No. 7 pp. 297 - 317 (2023)

Egyptian Journal of Chemistry

http://ejchem.journals.ekb.eg/

Promoting the Antimicrobial Potency of Synthesized Azo-azomethine Triazole Ligand by Metal Complexing

Nagy A. Morsy[1,2], Mohamad M. Ebrahium[3]

[1]*Department of Biochemistry, College of Science, University of Jeddah, Jeddah, Saudi Arabia*

[2]*Chemistry of Natural Compounds Department, National Research Centre, P.O. 12622, Dokki, Cairo, Egypt*

[3]*Department of Chemistry, College of Science and Arts at Khulais, University of Jeddah, Jeddah, Saudi Arabia*

Abstract

The novel azo-azomethine ligand incorporating oxygen and nitrogen donating atoms was designed and prepared. Additionally, a series of metal complexes derived from this azo-azomethine ligand namely, 2-(((1H-1,2,4-triazol-5-yl)imino)methyl)-5-((4-nitrophenyl)diazenyl)phenol formulated as $[Ru(HL)_2Cl(H_2O)].4H_2O$, $[M(HL)XYZ(H_2O)].nH_2O$, (where $M=Fe^{3+}$, Ni^{2+}, Co^{2+}, Mn^{2+}, Cu^{2+}**(8-10),** Zn^{2+} or UO_2^{2+}; X= Cl, CH_3COO or NO_3; Y= Cl, H_2O or 0; Z=H_2O or 0; n= 2, 0 or 7, $[VO(H_2L)_2(H_2O)].SO_4$ and $[Cu(H_2L)_2(H_2O)_2].SO_4$ were synthesized. The azo-azomethine ligand and its metallic chelates were structurally characterized based on thermal, elemental analyses and spectroscopic tools (Infrared, electronic absorption, nuclear magnetic resonance) as well as mass spectrometry, magnetic susceptibility, and molar conductivity measurements. The global reactivity descriptors, molecular electrostatic potential image, optimized geometry, lowest un-occupied and highest occupied molecular orbital (LUMO & HOMO) of the molecules were studied basing on density functional theory level (DFT) using B3LYP method and 6-311G.(d,p) basis set. The measurements were explored that the azo-azomethine ligand (**H_2L**) performed as monobasic or neutral bidentate ligand bonded the cations via the protonated/deprotonated phenolic oxygen atom and azomethine nitrogen atom adopting tetrahedral or distorted octahedral geometries around the cations. The in vitro microbicide activity showed that the azo-azomethine ligand (**H_2L**) was inactive while the complexes have a moderate inhibitory effect and some complexes showed activities close to the effect of standard drugs used.

Keywords: Azo-Schiff base, DFT, metal complexes, microbicide activity, Azo-aldehyde.

1. Introduction

Coordination chemistry has become one of the treasures in finding new biologically and pharmacologically active compounds. It is a new valuable source of synthetic and semisynthetic drugs that improves the activities of drugs [1]. The azo-azomethines which produced from the combination of azo-dyes moiety (-N=N-) with Schiff-base incorporating functionality azomethine linkage (-C=N-) [2]. The combination of two active moieties in one compound leads to enhance the physiochemical and biological characteristics of this flexibility class of chelators and their respective chelated complexes [3]. The medicinal activities of azo-compounds were revealed in Prontosil, a sulphonamide connected azo-dye, employed as a drug versus microbial diseases [4-6]. The biological activities of azo-compounds became the centre of an interest because of their behaviour as potential anticancer [7], anti-oxidant [8], antiviral (HIV) [9], anti-inflammatory [10], fungicidal [11], and bacteriostatic agents [12]. The azo-azomethines with characteristic azomethine moiety were attracted the interest of many scientists because of their antiproliferative, analgesic, anti-

*Corresponding author e-mail: nmorsy@uj.edu.sa; (Nagy A. Morsy).
EJCHEM use only: Received date 12 July 2022; revised date 04 September 2022; accepted date 02 October 2022
DOI: 10.21608/EJCHEM.2022.150062.6497

inflammatory [13], antitumor [14-17], antiepileptic [18], antidepressant [19] anti-oxidant [14-16], antidiabetic [20], enzyme & protein inhibitor, herbicidal and microbicide effect versus bacteria, fungi [16, 21] and many viruses (HIV, influenza A, COVID-19 and adenovirus) [22]. Cu^{2+} complexes of azomethine ligand were informed to safeguard the gut tract of human against ulcer through course of intensive medications and regard as an anti-arthritis drug [23]. Additionally, the pharmacological effectiveness of sulphonamide basing drugs was enhanced by converting them into Schiff bases. The azomethine linkage add a new feature that enhance the biological activities by facilitating the entering into the cells' environment [24]. In particular, the recent research directed to preparation of azo-azomethines and their coordinated compounds with a variety of metals (e.g. Hg, Pd, Pt, Zn, Cu, Ni, Co, Fe, Cr and V) and evaluation their anti-microbial activity [25, 26]. The importance of this class of compounds have been attributed to their easy synthetic reactions, diversity of the structures of their raw materials, duality of functional groups which improve the pharmacological characteristics. The present work studies the metal complexes of novel azo-azomethine incorporating both the azo (N=N) and azomethine (C=N) linkages. So this paper devoted to the preparation, and characterization of novel azo-azomethine ligand namely, 2-((1H-1,2,4-triazol-5-yl)imino)methyl)-5-((4-nitrophenyl)diazenyl)phenol **(H_2L, 1)**. In addition, its structure was elucidated using NMR, IR, and UV-Vis. Spectroscopies and mass spectrometry. Consequently, this azo-azomethine ligand was utilized to synthesis **Ru^{3+}**, **Fe^{3+}**, **VO^{2+}**, **UO_2^{2+}**, **Ni^{2+}**, **Co^{2+}**, **Mn^{2+}**, **Cu^{2+}** and **Zn^{2+}** complexes (Scheme 1). The synthesized complex's structure was elucidated by various spectroscopic, analytical, and thermal techniques as well as theoretical calculations. Auxiliary, DFT at B3LYP level of theory and 6-311G(d,p) basis set was utilized to discover charge distribution, optimized geometry, molecular electrostatic potential (MEP), and molecules' chemical reactivity. In addition, the investigation of the antimicrobial activities of the prepared azo-azomethine have been investigated. The target of this work was searching for novel potent antimicrobial compounds to overcome of the antimicrobial resistance problem of most of the drugs used.

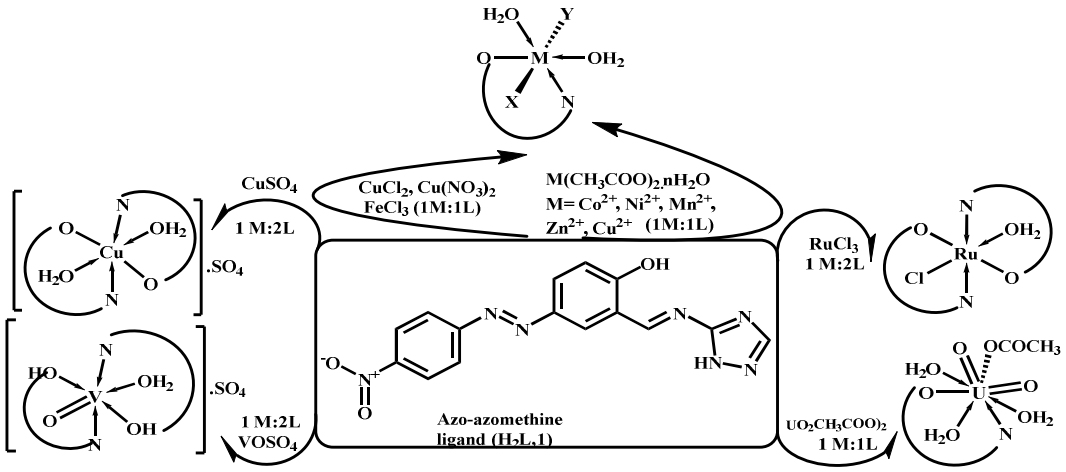

Scheme 1: Scheme for the prepared compound

2. EXPERIMENTAL

2.1. Physical and analytical measurements

The 1H-1,2,4-triazol-5-amine, DMSO, metal salts, and absolute ethanol (assay = 98.0-99.9%) were purchased from Merck or Sigma-Aldrich and utilized without further purification. A published method was used to prepare azoaldehyde, 2-hydroxy-5-((4-nitrophenyl)diazenyl) [27]. The analyses of the elements (N,H,C) for the azo-azomethine ligand and its chelated complexes was examined in laboratory of Micro-Analytical, Cairo University, Egypt, whereas the contents of metal (Ru^{3+}, Fe^{3+}, VO^{2+}, Ni^{2+}, Co^{2+}, Mn^{2+}, Cu^{2+}, Zn^{2+}) and Cl^- ions were examined by standard analytical methods [28, 29]. KBr plates was utilized to measure the IR spectra on a Perkin–Elmer-1430 infrared spectrophotometer over a range of 400 - 4000 cm^{-1}, National Research Centre, Egypt. The 1-cm quartz cell was employed to measure the electronic absorption spectra in DMSO over a range of 200 - 1100 nm on a SHMADZU 2600 spectrophotometer, University of Jeddah, Saudi Arabia. The mass spectrometry was measured on

JEUL JMS-AX-500 mass spectrometer while the NMR spectrum in DMSO-d_6 was measured on a JEOL EAC-500 spectrometer at National Research Centre, Egypt. The complexes TG analysis was measured on a Perkin Elmer 7 thermal analyzer over a range of 25 to 800 °C with heating rate 10 ºC/min, El-Menoufia University, Egypt. Gouy Matthey Balance was employed to record the magnetic susceptibility at 25 °C and calculated by the published equation [30]. The complexes molar conductance (10^{-3} M/DMSO) was assessed by Tacussel type CD6NG conductivity bridge was calculated by the published equation [31]. Unfortunately, several attempts to obtain a single crystal were unsuccessful, The purity of all prepared was checked by TLC.

2.2. Synthesis of azo-azomethine ligand (H_2L)

The azo-azomethine, ((1H-1,2,4-triazol-5-yl)imino)methyl)-5-((4-nitrophenyl)diazenyl) phenol **(H_2L, 1)** was synthesized by refluxing for five hours a mixture 2-hydroxy-5-((4-nitrophenyl)diazenyl) benzaldehyde (271 mg, 1 mmol, 30 mL of EtOH) and 1H-1,2,4-triazol-5-amine (84 mg, 1 mmol, 50 mL EtOH) in presence of 0.1 mL glacial CH_3COOH. Then let the reaction mixture to cool at 25 °C, when the coloured solid formed, separate it and wash it with EtOH, and dried in the vacuum to get the azo-azomethine (**H_2L, 1**) (309.4 mg, 0.918 mmol, 91.8%) (**Figure 1**) as a yellowish brown solid, m.p. 255 °C. Elemental analysis (Anal.) for $C_{15}H_{11}N_7O_3$ (337.30 g /mol): Found (calc.) %C 53.21 (53.41), %H 301 (3.29), %N 29.37 (29.07). FT-IR (KBr, cm^{-1}), 3505 $\nu(^{25}O\text{-}H^{36})$, 3309 $\nu(^{33}N\text{-}H^{35})$, 3088w, 2995w, 2900w ν(C-H), 1666 $\nu(^{26}C{=}N^{27})$, 1600 $\nu(^{29}C{=}N^{32})$& $\nu(^{30}C{=}N^{34})$, 1475 $\nu(^{11}N{=}N^{15})$, 1247 $\nu(^{23}C\text{-}O^{25})$, 1011 $\nu(^{32}N\text{-}N^{34})$, 1533, 1321 $\nu(^{12}NO_2)$. ^{1}H-NMR (DMSO-d_6, 500 MHz,): δ(ppm) = 8.47, 14.17 (s, 1H, NH^{31}), 10.32 (s, 1H, OH^{29}), 7.99 (d, 2H, C-$H^{8\&9}$), 8.35 (m, 1H, $CH^{7\&10}$), 8.18 (d, 1H, CH^{22}), 8.07 (d, 1H, CH^{24}), 7.16 (s, H, CH^{20}), 9.51 (s, H, CH^{28}), 8.35 (s, H, CH^{33}). ^{13}C-NMR (DMSO-d_6/150 Mhz): δ(ppm) = 148.63 (C6), 125.38 (C1&5), 123.76 (C2&4), 155.81 (C3&16), 119.19 (C18), 130.53 (C21), 123.76 (C19), 165.18 (C23), 118.66 (C17), 164.59 (C26), 163.62 (C30), 145.67 (C32).

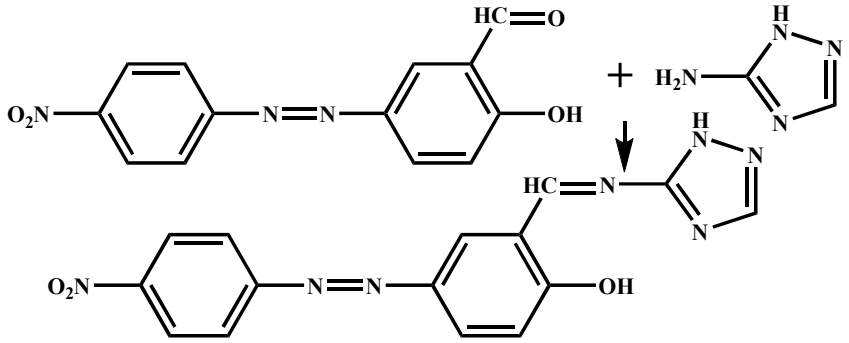

Figure 1: Synthesis of the 2-((1H-1,2,4-triazol-5-yl)imino)methyl)-4-((4-nitrophenyl)diazenyl)phenol (H_2L, 1)

2.3. Preparation of complexes (2-13)

Fe^{3+}(3), **Ni^{2+}(5)**, **Co^{2+}(6)**, **Mn^{2+}(7)**, **Cu^{2+}(8-10)**, **Zn^{2+}(12)**, **UO_2^{2+}(13)** complexes were synthesized by refluxing an equimolar amounts of the following salts ethanolic solution (50 mL): $FeCl_3{\cdot}6H_2O$ (271.3 mg), $Ni(CH_3COO)_2{\cdot}4H_2O$ (248.8 mg), $Co(CH_3COO)_2{\cdot}4H_2O$ (249.1 mg), $Mn(CH_3COO)_2{\cdot}4H_2O$ (245.1 mg), $Cu(CH_3COO)_2{\cdot}2H_2O$ (199.7 mg), $Cu(NO_3)_2.3H_2O$ (241.6 mg), $CuCl_2.2H_2O$ (170.5 mg), $Zn(CH_3COO)_2{\cdot}2H_2O$ (219.5 mg), and $UO_2(CH_3COO)_2{\cdot}2H_2O$ (424.2 mg) with ((1H-1,2,4-triazol-5-yl)imino)methyl)-4-((4-nitrophenyl)diazenyl)phenol (337.3 mg, 30 mL of EtOH). The refluxing continued for four hours with stirring. The resultant solid-colored complexes separated out, on heating and rinse out various times with hot EtOH and ultimately dried in vacuum over P_4O_{10}. The **Ru^{3+}(2)**, **VO^{2+}(4)** and **Cu^{2+}(11)** were prepared by the same procedure but in molar ratio 1M:2L using the following salts: $RuCl_3{\cdot}6H_2O$ (261.7 mg), $VOSO_4{\cdot}3H_2O$ (217.0 mg) $CuSO_4{\cdot}3H_2O$ (249.7 mg).

2.3.1. Ru^{3+}-complex (2): Yield (61.5%), color: dark brown, m.p.=277 °C, molar conductance (Λ_m) = 16.1 $ohm^{-1}cm^2mol^{-1}$, μ_{eff} = 1.63. Anal. for $[Ru(HL)_2Cl(H_2O)].4H_2O$, $C_{30}H_{26}RuN_{14}O_{11}Cl$, (899.18 g/mol): Found (calc.) %C 40.37(40.07), %H 3.16(3.36), %N 21.66(21.81), %Cl 3.77 (3.94), %Ru 10.99 (11.24). FT-IR (KBr, cm^{-1}), 3437 $\nu(H_2O)$, 3309 $\nu(^{33}N\text{-}H^{35})$, 3090w, 2955w, 2890w ν(C-H), 1637 $\nu(^{26}C{=}N^{27})$, 1601 $\nu(^{29}C{=}N^{32})$&$\nu(^{30}C{=}N^{34})$, 1470 $\nu(^{11}N{=}N^{15})$, 1273 $\nu(^{23}C\text{-}O^{25})$, 1010 $\nu(^{32}N\text{-}N^{34})$, 1534, 1306 ν ($^{12}NO_2$), 632 (^{25}O-Ru), 475 $\nu(^{27}N{\rightarrow}Ru)$.

2.3.2. Fe^{3+}-complex (3): Yield (65.6%), m.p.=287 °C, color: brown, Λ_m = 26.9 $ohm^{-1}cm^2mol^{-1}$, μ_{eff} = 6.08. Anal. for $[Fe(HL)Cl_2(H_2O)_2].2H_2O$, $C_{15}H_{18}FeN_7O_7Cl_2$, (535.10 g/mol): Found (calc.) %C 33.43(33.67), %H 3.15(3.39), %N 18.39(18.32), %Cl 12.98 (13.25), %Fe 10.00 (10.44). FT-IR (KBr, cm^{-1}), 3440 $\nu(H_2O)$, 3320 $\nu(^{33}N\text{-}H^{35})$, 3080w, 2934w,

2885w ν(C-H), 1613 ν(^{26}C=N^{27}), ν(^{29}C=N^{32})&ν(^{30}C=N^{34}), 1478 ν(^{11}N=N^{15}), 1280 ν(^{23}C-O^{25}), 1016 ν(^{32}N-N^{34}), 1531, 1296 ν ($^{12}NO_2$), 623 (^{25}O-Fe), 473 ν(^{27}N→Fe).

2.3.3. VO^{2+}-complex (4): Yield (61.8%), m.p.=290 °C, color: brown, Λ_m= 131.1 ohm^{-1}cm^{2}mol^{-1}, μ_{eff} = 1.66 BM. Anal. for $[VO(H_2L)_2(H_2O)].SO_4$, $C_{30}H_{24}VSN_{14}O_{12}$, (855.61 g/mol): Found(calc.) %C 41.89(42.11), %H 2.69(2.93), %N 22.60(22.92), %V 5.88(5.95). FT-IR (KBr, cm^{-1}), 3476 ν(^{25}O-H^{29}), 3288 ν(^{33}N-H^{35}), 3040w, 2940w, 2865w ν(C-H), 1623 ν(^{26}C=N^{27}), 1603 ν(^{29}C=N^{32})&ν(^{30}C=N^{34}), 1474 ν(^{11}N=N^{15}), 1274 ν(^{23}C-O^{25}), 1012 ν(^{32}N-N^{34}), 1522, 1319 ν($^{12}NO_2$), 1194, 977, 654 ν(SO_4), 933 (O=V), 592 (^{25}O→V), 498 ν(^{27}N→V).

2.3.4. Ni^{2+}-complex (5): Yield (58.9%), m.p.>300 °C, color: reddish brown, Λ_m = 14.9 ohm^{-1}cm^{2}mol^{-1}, μ_{eff} = 3.18 BM. Anal. for $[Ni(HL)(O)COCH_3(H_2O)]$, $C_{17}H_{15}NiN_7O_6$, (472.04 g/mol): Found(calc.) %C 43.40(43.26), %H 3.01(3.20), %N 20.51(20.77), %Ni 12.51(12.43). FT-IR (KBr, cm^{-1}), 3417 ν(H_2O), 3331 ν(^{33}N-H^{35}), 3060w, 2951w, 2888w ν(C-H), 1633 ν(^{26}C=N^{27}), 1600 ν(^{29}C=N^{32})&ν(^{30}C=N^{34}), 1490 ν(^{11}N=N^{15}), 1256 ν(^{23}C-O^{25}), 1015 ν(^{32}N-N^{34}), 1526, 1323 ν($^{12}NO_2$), 555 (^{25}O-Ni), 477 ν(^{27}N→Ni). 1580/1359(221) $\nu_s(CH_3COO)$/ $\nu_{as}(CH_3COO)(\Delta)$.

2.3.5. Co^{2+}-complex (6): Yield (67.6%), m.p.>300 °C, color: reddish brown, Λ_m = 7.9 ohm^{-1}cm^{2}mol^{-1}, μ_{eff} = 4.11 BM. Anal. for $[Co(HL)(O)COCH_3(H_2O)_3]$, $C_{17}H_{19}CoN_7O_8$, (508.31 g/mol): Found(calc.) %C 40.37(40.17), %H 3.63(3.77), %N 19.00(19.29), %Co 11.33(11.59). FT-IR (KBr, cm^{-1}), 3402 ν(H_2O), 3300 ν(^{33}N-H^{35}), 3045w, 2929, 2859w ν(C-H), 1616 ν(^{26}C=N^{27}), 1596 ν(^{29}C=N^{32})&ν(^{30}C=N^{34}), 1476 ν(^{11}N=N^{15}), 1266 ν(^{23}C-O^{25}), 1020 ν(^{32}N-N^{34}), 1532, 1313 ν($^{12}NO_2$), 520 (^{25}O-Co), 478 ν(^{27}N→Co). 1570/1340(230) $\nu_s(CH_3COO)$/ $\nu_{as}(CH_3COO)(\Delta)$.

2.3.6. Mn^{2+}-complex (7): Yield (67.6%), m.p.>300 °C, color: dark brown, Λ_m = 14.1 ohm^{-1}cm^{2}mol^{-1}, μ_{eff} = 5.88 BM. Anal. for $[Mn(HL)(O)COCH_3(H_2O)]$, $C_{17}H_{15}MnN_7O_6$, (468.29 g/mol): Found(calc.) %C 43.43(43.60), %H 3.32(3.23), %N 20.77(20.94), %Mn 11.61(11.73). FT-IR (KBr, cm^{-1}), 3431 ν(H_2O), 3298 ν(^{33}N-H^{35}), 3039w, 2956, 2870w ν(C-H), 1625 ν(^{26}C=N^{27}), 1607 ν(^{29}C=N^{32})&ν(^{30}C=N^{34}), 1469 ν(^{11}N=N^{15}), 1290 ν(^{23}C-O^{25}), 1014 ν(^{32}N-N^{34}), 1542, 1301 ν($^{12}NO_2$), 509 (^{25}O-Mn), 475 ν(^{27}N→Mn). 1587/1364(223) $\nu_s(CH_3COO)$/ $\nu_{as}(CH_3COO)(\Delta)$.

2.3.7. Cu^{2+}-complex (8): Yield (60.1%), m.p.=266 °C, color: dark brown, Λ_m = 8.8 ohm^{-1}cm^{2}mol^{-1}, μ_{eff} = 1.91 BM. Anal. for $[Cu(HL)(O)COCH_3(H_2O)]$, $C_{17}H_{15}CuN_7O_6$, (476.90 g/mol): Found(calc.) %C 42.64(42.82), %H 3.02(3.20), %N 20.09(20.36), %Cu 13.09(13.32). FT-IR (KBr, cm^{-1}), 3440 ν(H_2O), 3302 ν(^{33}N-H^{35}), 3049w, 2920, 2855w ν(C-H), 1622 ν(^{26}C=N^{27}), 1603 ν(^{29}C=N^{32})&ν(^{30}C=N^{34}), 1490 ν(^{11}N=N^{15}), 1253 ν(^{23}C-O^{25}), 1013 ν(^{32}N-N^{34}), 1524, 1323 ν($^{12}NO_2$), 520 (^{25}O-Cu), 466ν (^{27}N→Cu). 1569/1351(218) $\nu_s(CH_3COO)$/$\nu_{as}(CH_3COO)(\Delta)$.

2.3.8. Cu^{2+}-complex (9): Yield (66.6%), m.p.>300 °C, color: brown, Λ_m = 13.9 ohm^{-1}cm^{2}mol^{-1}, μ_{eff} = 1.88 BM. Anal. for $[Cu(HL)Cl(H_2O)]$, $C_{17}H_{15}CuN_7O_4$, (453.30 g/mol): Found(calc.) %C 39.52(39.75), %H 2.44(2.17), %N 21.50(21.63), %Cu 13.79(13.42). FT-IR (KBr, cm^{-1}), 3423 ν(H_2O), 3328 ν(^{33}N-H^{35}), 3034w, 2932, 2868w ν(C-H), 1643 ν(^{26}C=N^{27}), 1602 ν(^{29}C=N^{32})&ν(^{30}C=N^{34}), 1477 ν(^{11}N=N^{15}), 1275 ν(^{23}C-O^{25}), 1012 ν(^{32}N-N^{34}), 1521, 1304 ν($^{12}NO_2$), 511 (^{25}O-Cu), 449ν(^{27}N→Cu).

2.3.9. Cu^{2+}-complex (10): Yield (58.3%), m.p.>300 °C, color: brown, Λ_m = 28.1 ohm^{-1}cm^{2}mol^{-1}, μ_{eff} = 2.11 BM. Anal. for $[Cu(HL)NO_3(H_2O)]$, $C_{17}H_{15}CuN_8O_7$, (479.86 g/mol): Found(calc.) %C 37.68(37.55), %H 2.40(2.52), %N 23.46(23.35), %Cu 13.04(13.24). FT-IR (KBr, cm^{-1}), 3439 ν(H_2O), 3316ν ν(^{33}N-H^{35}), 3055w, 2911, 2866w ν(C-H), 1618 ν(^{26}C=N^{27}), 1601 ν(^{29}C=N^{32})&ν(^{30}C=N^{34}), 1478 ν(^{11}N=N^{15}), 1281 ν(^{23}C-O^{25}), 1015 ν ν(^{32}N-N^{34}), 1515, 1300 ν($^{12}NO_2$), 510 (^{25}O-Cu), 443ν(^{27}N→Cu). 1418, 1382, 945 ν (NO_3)(Δ=36).

2.3.10. Cu^{2+}-complex (11): Yield (61.8%), m.p.=280 °C, color: dark brown, Λ_m= 124.4 ohm^{-1}cm^{2}mol^{-1}, μ_{eff} = 1.74 BM. Anal. for $[Cu(H_2L)_2(H_2O)_2].SO_4$, $C_{30}H_{26}CuSN_{14}O_{13}$, (870.23 g/mol): Found(calc.) %C 41.09(41.41), %H 3.21(3.01), %N 22.07(21.85), %S 4.01(3.68), %Cu^{2+} 7.39(7.30). FT-IR (KBr, cm^{-1}), 3542 ν(^{25}O-H^{29}), 3430 ν(H_2O), 3313 ν(^{33}N-H^{35}), 3035w, 2936w, 2869w ν(C-H), 1612 ν(^{26}C=N^{27}), 1601 ν(^{29}C=N^{32})&ν(^{30}C=N^{34}), 1468 ν(^{11}N=N^{15}), 1255 ν(^{23}C-O^{25}), 1013 ν(^{32}N-N^{34}), 1529, 1324 ν($^{12}NO_2$), 1197, 989, 690 ν(SO_4), 533 (^{25}O→Cu), 488 ν(^{27}N→Cu).

2.3.11. Zn^{2+}-complex (12): Yield (62.1%), m.p.=295 °C, color: brown, Λ_m = 8.8 ohm^{-1}cm^{2}mol^{-1}, μ_{eff} = Dia. Anal. for $[Zn(HL)(O)COCH_3(H_2O)_3]$, $C_{17}H_{19}ZnN_7O_8$, (532.78 g/mol): Found(calc.) %C 38.60(38.33), %H 3.64(3.97), %N 18.33(18.40), %Zn 12.34(12.27). FT-IR (KBr, cm^{-1}), 3420 ν(H_2O), 3314 ν(^{33}N-H^{35}), 3061w, 2943, 2857w ν(C-H), 1619 ν(^{26}C=N^{27}), 1598 ν(^{29}C=N^{32})&ν(^{30}C=N^{34}), 1471 ν(^{11}N=N^{15}), 1267 ν(^{23}C-O^{25}), 1016 ν(^{32}N-N^{34}), 1523, 1313 ν($^{12}NO_2$), 583 (^{25}O-Zn), 474 ν(^{27}N→Zn). 1575/1358(217) $\nu_s(CH_3COO)$/ $\nu_{as}(CH_3COO)(\Delta)$. ^{1}H-NMR (300 MHz, DMSO-d_6): δ(ppm) = 8.47 (s, 1H, N*H*^{31}), 7.96 (d, 2H, C-H$^{8\&9}$), 8.31 (m, 1H, CH$^{7\&10}$), 8.05 (d, 1H, CH^{22}), 7.88 (d, 1H, CH^{24}), 7.43 (s, H, CH^{20}), 8.89 (s, H, CH^{16}), 1.87 (s, 3H, CH_3COO).

2.3.12. UO_2^{2+}-complex (13): Yield (70.1%), m.p.=288 °C, color: **brown**, Λ_m = 8.8 ohm^{-1}cm^{2}mol^{-1}, μ_{eff} = Dia. Anal. for $[UO_2(HL)(O)COCH_3(H_2O)].7H_2O$, $C_{17}H_{29}UN_7O_{15}$,

(809.43 g/mol): Found(calc.) %C 24.82(25.22), %H 3.72(3.61), %N 11.94(12.11), %U 29.11(29.65). FT-IR (KBr, cm^{-1}), 3452 ν(H_2O), 3331 ν(^{33}N-H^{35}), 3046w, 2972, 2932, 2779w ν(C-H), 1612 ν ν(^{26}C=N^{27}), 1600 ν(^{29}C=N^{32})&ν(^{30}C=N^{34}), 1473 ν(^{11}N=N^{15}), 1263 ν(^{23}C-O^{25}), 1017 ν(^{32}N-N^{34}), 1524, 1316 ν($^{12}NO_2$), 948 ν(O=U), 577 ν(^{25}O-U), 476 ν(^{27}N→U). 1588/1378(210) $\nu_s(CH_3COO)$/ $\nu_{as}(CH_3COO)(\Delta)$.

2.4. Theoretical calculations

The quantum chemical parameters were calculated by Density Functional Theory (DFT) employing Gaussian 09 Rev. A.02-MSP package program [32], and Gauss View Rev. 5.0.9 software was employed to imagine the found data [33]. The azo-azomethine **(H_2L)** molecular structure in the ground state has been optimized utilizing the DFT with Beckee3eLeeeYangeParr (B3LYP) functional levels for the 6-311G(d,p) basis set [34, 35].

2.5. Antimicrobial assessment

The assessment of *in-vitro* antimicrobial activity of the synthetics **(1-13)** was performed utilizing agar well diffusion technique versus different microbial species as *Aspergillus niger (A. niger), Bacillus subtilis, (B. subtilis) and Escherichia coli, (E. coli)* [36, 37]. The species of fungi and bacteria were cultivated at pH 7.4 on Czapek Dox´s agar (CDA), and Mueller-Hinton agar correspondingly. The agar´s plates were incubated at 37°C for 24 h (bacteria), and 28°C for 4 days (*A. niger*). A negative (DMSO; 2% v/v) and positive controls (Tetracycline for bacteria and amphotericin B for fungi) was also involved for comparison. The appearance of inhibition regions indicates the antimicrobial action of the tested compounds. Consequently, the average of three independent replicates was calculated. While the activity index was calculated [14].

3. RESULTS AND DISCUSSION

The ligand, ((1H-1,2,4-triazol-5-yl)imino)methyl)-5-((4-nitrophenyl)diazenyl)phenol **(H_2L, 1),** was interacted with the salts of the following metallic cations **Ru^{3+}**, **Fe^{3+}**, **VO^{2+}**, **Ni^{2+}**, **Co^{2+}**, **Mn^{2+}**, **Cu^{2+}**, **Zn^{2+}**, **UO_2^{2+}** leading to the formation of coordination compounds with the following general formulae $[M(HL)XYZ(H_2O)].nH_2O$ (where M= **Fe^{3+}(3)**, **Ni^{2+}(5)**, **Co^{2+}(6)**, **Mn^{2+}(7)**, **Cu^{2+}(8-10)**, **Zn^{2+}(12)** and **UO_2^{2+}(13),** X= Cl, NO_3 or CH_3COO and Y= Cl, or H_2O, Z= H_2O and n= 0, 2 or 7); $[M(H_2L)(H_2O)_2].SO_4$ where M= **VO^{2+}or Cu^{2+}** X=Y=H_2O and $[Ru(HL)_2Cl(H_2O)].4H_2O$. The structure of the prepared compounds was elucidated analytically, theoretically, thermally and by several spectroscopical tools, such UV-Vis., NMR, and FT-IR as well as mass spectrometry. The data of different measurements and theoretical calculation were recorded in the experimental section in Tables 1-3 and Tables S1-S5. The elemental analyses and mass spectrometry agreed with the proposed molecular formulae and confirmed that **Fe^{3+}, Ni^{2+}, Co^{2+}, Mn^{2+}, Cu^{2+}(8-10), Zn^{2+},** and **UO_2^{2+}** complexes formed in (1L:1M) molar ratio however the **Ru^{3+}, VO^{2+}** and **Cu^{2+}(11)** complexes formed in (2L:1M) molar ratio (Figures 2-4). The **Ru^{3+}, Fe^{3+}, Ni^{2+}, Co^{2+}, Mn^{2+}, Cu^{2+}(8-10), Zn^{2+},** and **UO_2^{2+}** complexes solutions (10^{-3} M/DMSO) have molar conductance value ranged from of 7.9–33.2 $\Omega^{-1}mol^{-1}cm^2$, indicative to the non-electrolyte nature of the prepared complexes and the Cl^-, NO_3 or CH_3COO anions are squarely connected to the cations [38]. The markedly high value of a few complexes could be owing to the partial solvolysis by DMSO molecules [38]. Nevertheless, the **VO^{2+}** and **Cu^{2+}(11)** have molar conductance values equal to 131.2 and 124.2 $\Omega^{-1}cm^2mol^{-1}$ respectively, denoting to the electrolytic nature of these complexes. These molar conductance values are acceptable with the work of Young el al. which proposed the range for 2:1 electrolyte in DMF is 110-150 $\Omega^{-1}cm^2mol^{-1}$ [39].

$[M(HL)XYZ(H_2O)].nH_2O$

M=Fe^{3+}, X=Y=Cl, Z=H_2O, n=2	**(3)**
M= Ni^{2+}, X=CH_3COO, Y=Z=n= 0	**(5)**
M= Co^{2+}, X=CH_3COO, Y=Z=H_2O, n = 0	**(6)**
M= Mn^{2+}, X=CH_3COO, Y=Z=n= 0	**(7)**
M= Cu^{2+}, X=CH_3COO, Y=Z=n= 0	**(8)**
M= Cu^{2+}, X=Cl, Y=Z=n= 0	**(9)**
M= Cu^{2+}, X=NO_3, Y=Z=n= 0	**(10)**
M= Zn^{2+}, X=CH_3COO, Y=Z=H_2O, n =0	**(12)**

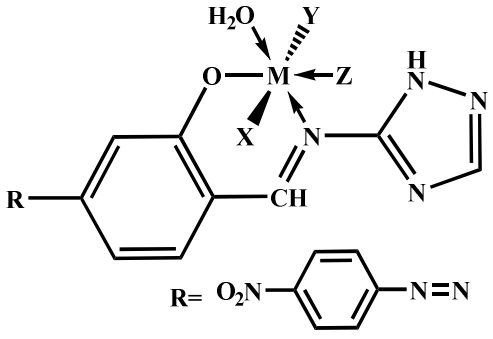

Figure 2: Structure of Fe^{3+}, Ni^{2+}, Co^{2+}, Mn^{2+}, Cu^{2+}, Zn^{2+}, and UO_2^{2+} complexes (3), (5-10) and (12)

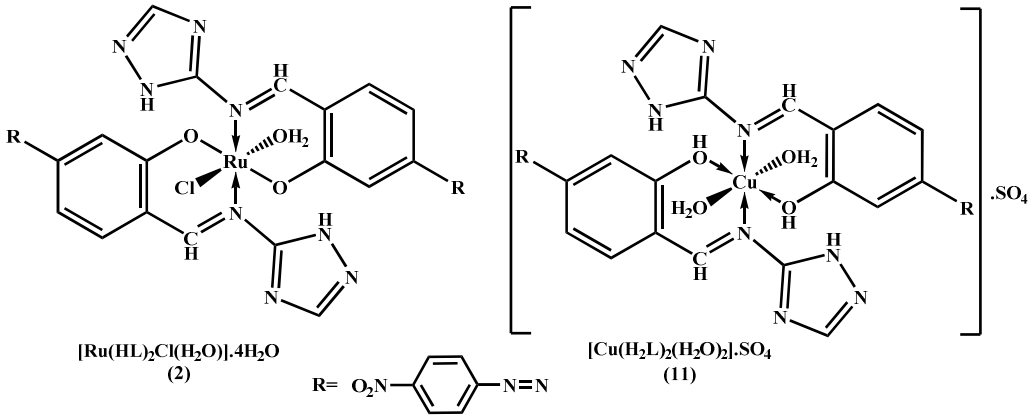

Figure 3: Structure of Ru^{3+}, and Cu^{2+} complexes (2) and (11)

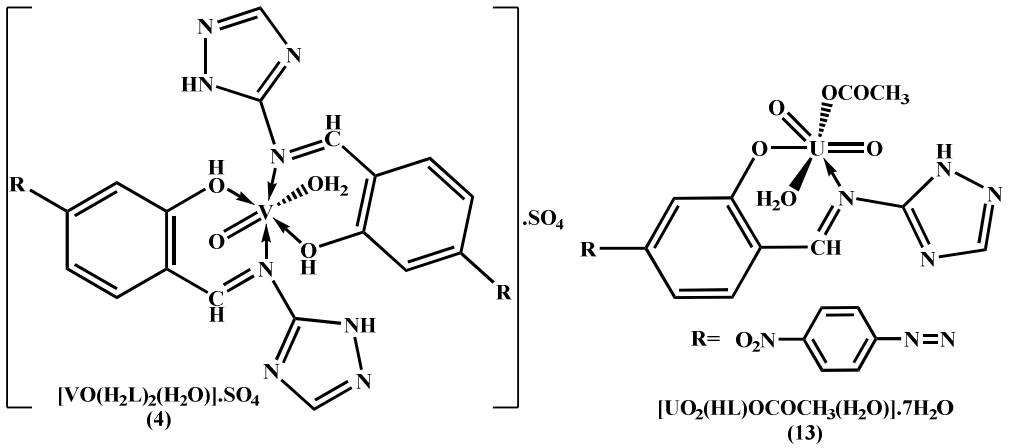

Figure 4: Structure of VO^{2+}, and UO_2^{2+} complexes (4) and (13)

3.1. Spectroscopic studies

3.1.1. IR spectra

In the experimental section, the IR spectral information was presented. The azo-azomethine IR spectrum displayed two medium bands at 3505, 3309 cm^{-1} which could be allocated to the hydroxyl υ(O-H) and υ(N-H) groups respectively while the two strong bands observed at 1666, 1600 cm^{-1} may be allotted to the azomethine groups of Schiff base and triazole moieties. The medium bands which observed at 1475, 1307 and 1030 may be mapped to the following linkages azo (N=N), phenolic (C-O) and (N-N) of triazole moiety congruently. By comparing the infrared data of complexes to that of free azo-azomethine (H_2L, 1) Table S1, the coordination mode of azo-azomethine (H_2L, 1) can be determined. From this comparison we can conclude that the azo-azomethine **(H_2L,1)** interacted with different metallic cations in one of the following two modes. Firstly, it interacted with **Ru^{3+}**, **Fe^{3+}**, **Ni^{2+}**, **Co^{2+}**, **Mn^{2+}**, **Cu^{2+}(8-10), Zn^{2+}** and **UO_2^{2+}** as uni-negative bidentate ligand linked covalency the metallic cations via deprotonated phenolic hydroxyl group (O^{25}) and chelated via the azomethine nitrogen atoms (N^{27}). This chelation mode was authenticated from the next observations. i) The disappearing of stretching frequency of phenolic hydroxyl group ν(OH) with simultaneous positive shift of phenolic linkage (C-O) by 17-54 cm^{-1} [40]. ii) the negative shift in the stretching frequency of Schiff base azomethine group (C=N) by 23-54 cm^{-1}.) the appearance of new stretching frequencies in the 510- 632 and 433-498 cm^{-1} ranges which could be inductive to the ν(^{25}O-M) and ν(^{27}N→M) congruently [41]. In the second manner, The azo-azomethine **(H_2L,1)** interacted with **VO^{2+}** and **Cu^{2+}(11) ions** as a neutral bidentate ligand in which the coordination took place via the protonated hydroxyl (^{25}O) and Schiff base azomethine (^{27}N) groups. This chelation manner was authenticated from the nest remarks. i) the negative shift in the stretching frequency of phenolic hydroxyl group with simultaneous positive shift of phenolic

linkage (C-O) [40]. ii) the negative shift in the stretching frequency of Schiff base azomethine group (C=N) by 23-54 cm^{-1}. iii) the appearance of new stretching frequencies at 592, 533 and 498, 488 cm^{-1} which could be inductive to the $\nu(^{25}O\rightarrow M)$ and $\nu(^{27}N\rightarrow M)$ congruently [41]. In **Ni^{2+}**, **Co^{2+}**, **Mn^{2+}**, **Cu^{2+}(8), Zn^{2+}** and **UO_2^{2+}** complexes the appearance of two distinctive stretching frequency bands in the 1569-1588 cm^{-1} and 1340-1358 cm^{-1} ranges may be ascribed to $\upsilon_{as.}(COO^-)$ and $\upsilon_{sy.}(COO^-)$ congruently, signifying that the acetate group participated in the chelation with metallic cations. The coordination mode of acetate group can be determined based on the magnitude of the difference between the $\upsilon_{as}(COO^-)$ and $\upsilon_{sy.}(COO^-)$. The differences between the two stretching frequency bands ($\Delta= \nu_{as}-\nu_s$) were ranged from 210 to 230 cm^{-1} which is suggesting that the acetate anions bonded to metallic caions as a monodentate fashion [42, 43]. The **VO^{2+}** and **Cu^{2+}(11)** complexes displayed three stretching frequency bands at 1194, 977 634 and 1197, 989, 690 cm^{-1} distinctive to the ionic sulphate group of the two complexes respectively. This result was further emphasized from their high molar conductance values [42, 44]. The nitrato **Cu^{2+}(10)** complex displayed three bands at ν_5(1418), ν_1(1382) and ν_2(903) implying that the nitrate anion participated in the chelation process. The difference between the two high absorption frequency bands (ν_5-ν_1) is 36 cm^{-1} means that, the nitrate anions attached to the Cu^{2+} cation as uni-dentate chelator [42, 45]. In the FT-IR spectra of VO^{2+} and UO_2^{2+} complexes, there are new stretching frequency bands at 933 and 943 cm^{-1} which could be ascribed to the ν(V=O) and ν(O=U=O) [41, 46, 47]. The Literature indicates that the vibrations of aromatic C–H normally appear around 3000 cm^{-1} while the characteristic region for aliphatic C-H vibrations is extended from 2800 to 3000 cm^{-1}. Here, pure symmetric vibrational bands are seen in the 3034-3090, range assigned to the aromatic C–H while pure asymmetric and symmetric vibrational stretching bands for the aliphatic C-H are noted in ranges extended from 2911 to 2995 cm^{-1} and from 2856 to 2890 cm^{-1} [48]. The aromatic nitro group generally demonstrated symmetric and asymmetric stretching vibrations bands in the 1550–1500 and 1360–1290 cm^{-1} ranges. In our compounds the first band was shown in the 1515-1542 cm^{-1} range while the second band was shown in the range extended from 1296 to 1323 cm^{-1}. The C-NO_2 stretching of aromatic nitro compound cannot be assigned correctly in the finger-print region due to the crowding of bands [49].

3.1.2. Nuclear magnetic *resonance* (NMR)

To attain useful information about the azo-azomethine **(H_2L,1)** structure and recognize the hydrogen bonding as well as determine its coordination mode with the metallic cations. The ^{1}H and ^{13}C NMR spectra were carried out in DMSO-d_6 and their chemical shifts is summarized in section 2.2 and explained, basing on the atom labelling in **Figure 6**. In ^{1}HNMR the disappearance of aldehyde proton of the reactant at ≈ 9.9 ppm indicates the formation of the imine group between the amine moiety of the triazole and the aldehyde moiety of the diazenyl reactants. In addition, the disappearance of aldehyde carbon at ≈190 ppm of the reactant in ^{13}CNMR and it is replaced with up field carbon at 164.59 ensured the formation of imine moiety in the ligand [50, 51]. In ^{1}HNMR (**Figure S1**), the compound has three exchangeable protons at 8.47 , 14.17 and 10.32 and which assigned to the protons of NH and the hydroxyl proton that indicted by the decrease of the signal intensity with changing the solvent from DMSO to DMSO+D_2O. ^{1}HNMR indicated the presence of one downfield proton at 9.52, which could be ascribed to the methine proton produced from the imine formation. In addition, the overlapping CH signals appeared at 7.16 – 8.35 ppm ascribing to the aromatic protons of the two phenyl rings. The noted chemical shift of H^8, H^9, H^{22} (δ = 7.99, 8.18 ppm) is a characteristic downfield value of protons in *o*-position for the diazinyl moiety, whereas the downfield shift of the singlet peak of H^{24}(8.07) and the up-filed shift of H^{20} (7.16) suggested the presence of the hydroxyl group at ortho and meta positions to these two protons respectively [52-54]. The proton of the triazole ring appears at 8.35 ppm and a characteristic exchangeable proton of OH appears at 10.32. It coincided with the downfield value of C-23 at 165.18 ppm in the aromatic benzene ring due to the presence of OH at C-23. The ^{1}H-NMR spectrum Zn^{2+} complex (**Figure S2**), showed that the chemical shift of the hydroxy proton (^{36}H-O^{25}) is disappeared at the implying that the hydroxyl group took part in the chelation to the metallic ions in its deprotonated form which supported the suggested mode of chelation. In ^{13}C-NMR (Figure S3), the number of carbons is 15 carbons. The two carbons of triazole ring appears at 163.62 and 145.67 ppm. The carbon of the aromatic rings appears at 118.66–165.18. The assignment of carbon and protons is confirmed by comparing with similar compounds [55]. The two exchangeable protons at 8.47 and at 14.17 ppm can be attributed to the NH protons which refers to the anti- and syn-configurations of the ligand around C=N. therefore, the ligand formed is a mixture as shown in **Figure 5.** From the size of the two signals, we can conclude that the most abundant one is the anti-structure [56].

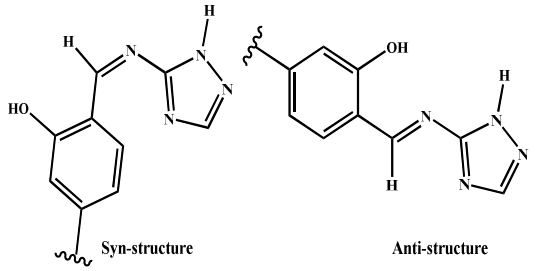

Figure 5: The Syn- and Anti-structures of azo-azomethine ligand (H_2L, 1)

3.1.3. Mass spectrometry (MS) of azo-azomethine (H_2L, 1)

The MS for azo-azomethine **(H_2L, 1) (Figure S4)** proved the anticipated structure with molecular ion peak (M^+) at 337 m/z in EI-mass. Additionally, many peaks of fragments appeared in the mass spectrometry conforming the structure. The ligand revealed fragments at 321, 292, 270, 243, 186, 150, 122, 97 and 94 m/z it could be explained as follow. the two fragment (a&b) at m/z 321 and 292 may be due to the missing phenolic hydroxyl and nitro group from the azo-azomethine molecule while the fragment (c) at m/z =269 may be assigned to the 2-(iminomethyl)-4-((4-nitrophenyl)diazenyl)phenol fragment which resulted from the losing of triazole moiety. Secondly the fragment (d) at m/z =243 may be assigned to the 3-((4-nitrophenyl)diazenyl)phenol fragment. In addition, the fragments 186, 150, 122 and 94 m/z may be attributed to the fragments 2-(((1H-1,2,4-triazol-5-yl)imino)methyl)phenol, 1-(4-nitrophenyl)-2l2-diazene, nitrobenzene, and N-(1H-1,2,4-triazol-5-yl)methanimine respectively. The other fragment which appeared at m/z =67 may be assigned to triazole moiety as shown in (Figure S5). The mass spectrometry of Ru^{3+}, VO_2^{2+}, Cu^{2+} and Cu^{2+} complexes (2), (4), (10) and (11) confirm the molecular weight of these complexes ($C_{17}H_{19}ZnN_7O_8$) as it showed the presence of molecular ion peak ($M^{+\bullet}$) at 890, 855, 479 and 870 m/z in EI-mass.

3.1.4. Electronic absorption spectroscopic (EAS) and magnetic moment (μ_{eff}) measurements.

The structure of the azo-azomethine **(H_2L,1)** uncovered that the two lone pairs of electrons in the azo group are not only interacting nonbonding electrons, but that the azo-azomethine also contains nitro group, which could be another source of lone pair electrons. Thus, other n→π* transition is anticipated to happen from these non-bonding orbitals to different π* molecular orbital spreading over such a large molecule [57]. The EAS of azo-azomethine (**H_2L, 1**) and its metallic complexes **(1-13)** were determined in DMSO and itemized in Table 1. In the UV and visible regions, the EAS of azo-azomethine (**H_2L, 1**) divulged three sets of bands. The first of the shortest wavelengths at 264 and 279 nm could be specified to the π→π* transition in the phenyl moieties and intra ligand π→π* transition [58]. The second set at 313 and 379 could be inductive to the n→π* transition of the azomethine groups of the Schiff base moiety and triazole moiety [58]. The third set appeared in the visible region at 446 and 568 nm may possibly be corresponded to π→π* transition involving the azo group's π electron and π→π* transition involving the whole compounds' electronic system with a significant charge transfer feature resulting mostly from the phenolic moiety. The n-π* transitions of the complexes were shifted to some extent compared to the free ligand, most likely due to imino-nitrogen coordination to the metal ion [57]. Ru^{3+} ion has a $^2T_{2g}$ ground state with initially excited doublet levels in the order of decreasing energy are $^2T_{1g}$, and $^2A_{2g}$ which arise from $^4t_{2g}{}^1e_g$ configuration [59]. The hexa-chelated Ru^{3+} ions have two transition around 460 and 575 which assigned to the charge transfer ($L\pi y \rightarrow T_{2g}$) and $^2T_{2g} \rightarrow {}^2A_{2g}$ transitions [60] but due to the strong bands of azo linkage π→π* and charge transferer transitions, these two bands did not appear in the spectrum of this complex. The Ru^{3+} complex exhibits magnetic moment value equal 1.63 BM which is consistent with a spin-only value of low spin Ru^{3+} specie [45]. In octahedral symmetry for Fe^{3+} complexes the ground state (^6S) splits into $^6A_{1g}$ $^4T_{1g}(P)$, $^4T_{2g}$, $^4A_{1g}$ and $^4E_{1g}$ Thus in octahedral field three spin allowed bands corresponding to the following transitions $^6A_{1g}(S) \rightarrow {}^4T_{1g}(G)$(~950 nm), $^6A_{1g}(S) \rightarrow {}^4T_{2g}(G)$(~600 nm), $^6A_{1g}(S) \rightarrow {}^4A_{1g}(G)$ $^4E_{1g}(G)$(~450 nm) [61]. According to this explanation. The EAS for Fe^{3+} complex **(3)** demonstrated two peaks at 976, 611 nm referable to the $^6A_{1g}(S) \rightarrow {}^4T_{1g}(G)$ and $^6A_{1g}(S) \rightarrow {}^4T_{2g}(G)$ transitions respectively which is compatible with an octahedral geometry **(Figure 2)** [62]. The third band which appeared around 450 nm is not detectable, maybe vanished by the strong bands of azo linkage π→π* and charge transferer transitions. The μ_{eff} value of Fe^{3+} complex **(3)** at room temperature was found to be equal to 6.08 BM inductive to five un-paired electrons system and well-suited with high spin octahedral Fe^{3+} cations [63]. In hexa-coordinated VO^{2+} complexes the ground state $^2T_{2g}$ and ^2E_g splits into $^6B_{2g}$ ^2E_g and $^2B_{1g}$, $^2A_{1g}$ respectively thus in octahedral field three spin allowed bands corresponding to the following transitions $^2B_{2g}(d_{xy}) \rightarrow {}^2E_g(d_{xz},d_{yz})(\nu_1)$, $^2B_{2g}(d_{xy}) \rightarrow {}^2B_{1g}(d_{x2-y2})(\nu_2)$ and $^2B_{2g}(d_{xy}) \rightarrow {}^2A_{1g}(d_{z2})(\nu_3)$ respectively [62]. So the two peaks which appeared at 1048, 800 nm, in the EAS of VO^{2+} complex **(4)** is imputable to the transitions $^2B_2(d_{xy}) \rightarrow {}^2E_1(d_{xz},d_{yz})(\nu_1)$ and $^2B_2(d_{xy}) \rightarrow {}^2B_1(d_{x2-y2})(\nu_2)$ respectively [63]. These

transitions are compatible with an octahedral geometry for VO^{2+} cation **(Figure 4)** [64, 65]. The third band which is assigned to the $^2B_{2g}(d_{xy})\rightarrow{}^2A_{1g}(d_{z2})(\nu_3)$ is not noticeable, maybe vanished by the strong bands of azo linkage $\pi\rightarrow\pi^*$ and charge transferer transitions. This VO^{2+} complex displayed μ_{eff} value equal 1.80 BM that, is consistent with a spin-only value [64, 65] In tetrahedral symmetry for Ni^{2+} complexes $^3T_{2g}$ state term originating from ^3F level become ground state. Thus, in tetrahedral field, three spin allowable bands corresponding to the following transitions $(\nu_1)^3T_{1g}(F)\rightarrow{}^3T_{2g}(F)$ (2000 nm), $(\nu_2)^3T_{1g}(F)\rightarrow{}^3A_{2g}(P)$ (1000) and$(\nu_3)^3T_{1g}(F)\rightarrow{}^3T_{1g}(P)$ (625). The EAS for Ni^{2+} complex **(5)** showcased two peaks at 1088, 588 nm imputable to the $^3T_{1g}(F)\rightarrow{}^3A_{2g}(P)(\nu_2)$ and $^3T_{1g}(F)\rightarrow{}^3T_{1g}(P)(\nu_3)$ transitions respectively which is compatible with an tetrahedral skeleton **(Figure 2)** [64, 66]. The first band which is assigned to the $(\nu_1)^3T_{1g}(F)\rightarrow{}^3T_{2g}(F)$ (2000 nm), is not noticeable, because it is out of spectrophotometer scale. At room temperature, the μ_{eff} value of Ni^{2+} complex **(5)** was found to be 3.18 BM which is within the normal range for a high spin tetrahedral Ni^{2+} complexes and excluded the possibility of square planar structure [67]. In octahedral symmetry for Co^{2+} complexes, ground state (^4F) splits into $^4T_{1g}(P)$, $^4T_{2g}$ and $^4A_{2g}$ Thus in octahedral field, three spin permitted bands corresponding to the following transitions $(\nu_1)^4T_1g(F)\rightarrow{}^4T_{2g}(F)$, $(\nu_2)^4T_1g(F)\rightarrow{}^4A_{2g}$ and $(\nu_3)^4T_1g(F)\rightarrow{}^4T_{1g}(p)$.[64, 68] according to this description. The EAS for Co^{2+} complex **(6)** showed two peaks at 1094, 579 nm imputable to the $(\nu_1)^4T_1g(F)\rightarrow{}^4T_{2g}(F)$, and $(\nu_2)^4T_1g(F)\rightarrow{}^4A_{2g}$ transitions respectively which is compatible with an octahedral skeleton **(Figure 2)** [64, 68]. The low value of ν_1/ν_2 (1.89) related to the regular range for octahedral Co^{2+} complexes (1.95–2.48), suggests that it is distorted. This is consistent with the band broadness which attributed to the envelope of the electronic transitions from $^4E_g(^4T_{1g})$ to ^4E_g and $^4B_{2g}$ components of $^4T_{2g}$ in a tetragonally distorted octahedral setting [69]. The μ_{eff} of Co^{2+} complex **(6)** is 4.65 BM which is identical to three unpaired electrons and similar to a high spin Co^{2+} ion (d^7) [70]. The EAS of Mn^{2+} complex **(7)** did not display any band in the visible region due to the differences between multiplicities of ground and excited states as well as obscuration of the very weak d–d absorptions of the Mn^{2+} complexes by the high intense bands of azo linkage $\pi\rightarrow\pi^*$ and charge transferer transitions tailing into the visible region **(Figure 2)** [71]. The Mn^{2+} complex **(7)** has a magnetic moment values equal to 6.05 BM referable to a high-spin d^5 Mn^{2+} species [71].

Table 1

UV-Vis. spectra of the azo-azomethine (H2L) and its complexes (1-13)

No	Bands (nm) in DMSO	Electronic transition	μ_{eff} (BM)	Geometry
H_2L (1)	264, 279, 313, 376, 446, 568	$\pi\rightarrow\pi^*$, $n\rightarrow\pi^*$	--	
Ru^{3+}complex (2)	267, 281, 369, 407, 464, 539	$(L\pi y\rightarrow T_{2g})$ $^2T_{2g}\rightarrow{}^2A_{2g}$	1.63	distorted octahedral
Fe^{3+}complex (3)	266, 289, 322, 429, 560, 758, 1078	$(\nu_2)^6A_{1g}(S)\rightarrow{}^4T_{2g}(G)$ $(\nu_1)^6A_{1g}(S)\rightarrow{}^4T_{1g}(G)$	6.08	distorted octahedral
VO^{2+}complex (4)	266, 279, 338, 373, 541, 815, 1048	$(\nu_2)^2B_2(d_{xy})\rightarrow{}^2B_1(d_{x2-y2})$ $(\nu_1)^2B_2(d_{xy})\rightarrow{}^2E_1(d_{xz},d_{yz})$	1.80	distorted octahedral
Ni^{2+}complex (5)	268, 307, 425, 471, 528, 547, 585, 1088	$(\nu_3)^3T_{1g}(F)\rightarrow{}^3T_{1g}(P)$ $(\nu_2)\ ^3T_{1g}(F)\rightarrow{}^3A_{2g}(P)$	3.88	tetrahedral
Co^{2+}complex (6)	266, 299, 419, 468, 534, 579, 1094	$(\nu_2)^4T_1g(F)\rightarrow{}^4A_{2g}$ $(\nu_1)^4T_1g(F)\rightarrow{}^4T_{2g}(F)$	4.65	distorted octahedral
Mn^{2+} complex (7)	266, 290, 330, 431, 467, 543	$\pi\rightarrow\pi^*$, $n\rightarrow\pi^*$	6.05	tetrahedral
Cu^{2+} complex (8)	265, 292, 390, 438, 641, 1090	$^2B_{2g}(d_{xy})\rightarrow{}^2E_g(d_{dx2-y2})$, $^2B_{2g}(d_{xz,}\ d_{yz,})\rightarrow{}^2B_{1g}$, $^2A_{1g}(d_{dx2-y2}$, $d_{z2})$	2.11	tetrahedral
Cu^{2+} complex (9)	270, 300, 391, 435, 678, 1080		1.92	
Cu^{2+} complex (10)	269, 285, 388, 485, 718, 1074		1.99	

Cu^{2+} complex (11)	266, 293, 331, 414, 639, 1000	$^2B_{1g}(d_{x2-y2}) \rightarrow {}^2B_{2g}(d_{xy})$ $^2B_{1g}(d_{x2-y2}) \rightarrow {}^2A_{1g}(d_{z2})$	1.77	tetragonally distorted octahedral
Zn^{2+} complex (12)	264, 287, 331, 425, 461, 572	$\pi \rightarrow \pi^*$, $n \rightarrow \pi^*$	Dia.	--
UO_2^{2+} complex (13)	270, 280, 373, 395, 465, 542	$\pi \rightarrow \pi^*$, $n \rightarrow \pi^*$	Dia.	--

In The EAS of Cu^{2+} complexes **(8-10)** there are two well defined bands in the ranges extended from 1074-1090 and 641 to 718 nm. These bands are ascribable to the following transitions $^2B_{2g}(d_{xy}) \rightarrow {}^2E_g(d_{dx2-y2})$, $^2B_{2g}(d_{xz,}d_{yz,}) \rightarrow {}^2B_{1g}$, $^2A_{1g}(d_{dx2-y2}$, $d_{z2})$ which are typical for tetrahedral Cu^{2+}complexes **(Figure 2)**. In addition, the μ_{eff} value for these complexes ranged from 1.92-2.11 MB reinforces the anticipated geometry and is also associated with the lower symmetry of the complex's molecules [64, 72]. The Cu^{2+}Complex **(11)** is quite different than the others in respect to the layout of EAS and magnetic moment. The ground state and excited state of hexa-chelated Cu^{2+} ion (octahedral crystal field) is $t_{2g}^6e_g^3$ with ^2E_g term and $t_{2g}^5e_g^4$ with $^2T_{2g}$ term respectively. Consequently, the electronic transition expected is $^2E_g \rightarrow {}^2T_{2g}$. However, the octahedral arrangement is distorted due to the Jahn-Teller effect, which causes tetragonal symmetry in which the ^2E_g is split into $^2B_{1g}(d_{x2-y2})$ and $^2A_{1g}(d_{z2})$ levels while the $^2T_{2g}$ also splits into $^2B_{2g}(d_{xy})$ and $^2E_g(d_{xz},d_{yz})$ levels. Thus, three bands are anticipated for tetragonal (D_{4h}) symmetry viz. $^2B_{1g}(d_{x2-y2}) \rightarrow {}^2E_g(d_{yz,}d_{xz})$, $^2B_{1g}(d_{x2-y2}) \rightarrow {}^2B_{2g}(d_{xy})$, and $^2B_{1g}(d_{x2-y2}) \rightarrow {}^2A_{1g}(d_{z2})$ which may be found around 500, 650 and 1000 nm consecutively [62, 64, 68]. In Cu^{2+} complex **(11)**, the bands with a maxima at 1000 and 639 nm are assigned to the transitions $^2B_{1g}(d_{x2-y2}) \rightarrow {}^2A_{1g}(d_{z2})$ and $^2B_{1g}(d_{x2-y2}) \rightarrow {}^2B_{2g}(d_{xy})$. The third theoretically possible transition $^2B_{1g}(d_{x2-y2}) \rightarrow {}^2E_g(d_{yz,}$ $d_{xz})$ is not observable, perhaps being vanished by the strong frequency of azo linkage $\pi \rightarrow \pi^*$ transition. Furthermore, the μ_{eff} value for this complex was 1.77 MB which is close to 1.73 expected for a single unpaired spin and reinforces the octahedral geometry **(Figure 3)**. In EAS of UO^{2+} complex **(13)** theoretically thinkable transitions charge transfer from the ligand to the UO_2^{2+} ion (LMCT) and the charge transfer from the oxygen of the UO_2^{2+} moiety to the f-orbital of the U^{6+} ion (O→U) is not observable, perhaps being vanished by the strong bands of azo linkage $\pi \rightarrow \pi^*$ and charge transferer transitions.

3.1.5. Thermogravimetric analysis

The TG analysis is useful not only for determining the thermal stability of the complexes under investigation, but also to provide basic knowledge about the water molecule's nature by mass loss as a function of temperature. The thermogram of the isolated complexes were determined in a temperature ranged from 25 to 800 °C as listed in Table S4. The thermogram demonstrated notable decomposing continuous phases in the range of temperature from 25 to 564 °C which were completed with the formation of residues composed from metal oxide or metal oxide contaminated carbon. The consecutive decomposing stages could be explained as follows. The Fe^{3+} and Ru^{3+} complexes thermograms displayed four stages of mass loss. The first step for decaying happened in the range of temperature extended from 25 and 122 °C accompanied by mass loses of 7.89, 5.22% (calc. 8.01, and 6.73%) referring to the liberation of four and two hydrated water molecules respectively. The second step of decaying took place in the range of temperature extended from 100 to 240 °C matching with loss of one and two chelated water molecules with mass lose equal to 1.87, 7.08% (calc. 2.00, 6.73). The third step of decaying took place in the range of temperature extended from 233-335 °C matches to the dropping of one and two chloride ions associated with losing in mass equal to 3.76 and 12.89% (calc. 3.94 and 13.25%). The fourth step of decaying occurred in the range of temperature extended from 335-564 °C with losing in mass equal to 70.89, 54.95% (calc. 72.12 and 56.12) matching to the completion of complexes decomposition leaving Ru_2O_3 and Fe_2O_3+C correspondingly. The VO^{2+}, Ni^{2+}, Co^{2+}, Mn^{2+}, Cu^{2+}, Zn^{2+} and UO_2^{2+}complexes thermograms demonstrated three steps of mass loss. The first step of breakdown in VO^{2+}, Ni^{2+}, Co^{2+}, Mn^{2+}, Cu^{2+} and Zn^{2+} complexes signify to lose of one, two or three chelated water molecules in the range of temperature extended from 100 to 211 °C associated with mass dropping of 1.95.12, 3.82, 11.54, 3.45, 3.78, 3.75, 3.97, 4.14 and 10.67% (calc. 2.11, 4.01, 11.65, 3.85, 3.99, 3.55, 4.11, 4.00 and 10.14%) while in UO_2^{2+}complex the first step of breakdown denotes to the loss of seven hydrated water molecules at temperature extended from 20 to 85 °C related with mass dropping of 14.38% (calc. 14.91%). The second step of breakdown which occurs in range of temperature extended from 190-288°C associated with dropping in mass equal to 10.99, 12.59, 12.69, 12.12, 12.46, 12.92, 7.82, 11.03, 10.88, and 9.56% (calc. 11.22, 12.69, 12.49, 12.69, 12.00, 12.55, 7.55, 10.87, 11.16, and 9.16%) and it refers to the losing of anions in VO^{2+}, Ni^{2+}, Co^{2+}, Mn^{2+}, Cu^{2+} and Zn^{2+}

complexes or acetate ion plus coordinated water molecule in UO_2^{2+}complex. The third stage of decomposing happened in the range of temperature extended from 298-501 °C with losing in mass equal to 74.48, 67.77, 59.77, 67.55, 67.08, 66.75, 70.66, 75.69, 61.67 and 42.46% (calc. 76.05, 66.76, 58.42, 68.31, 68.00, 65.96, 70.06, 74.89, 63.43, 63.43 and 42.10%) matching to the completion of complexes decomposition leaving VO_2, NiO, CoO, MnO, CuO, ZnO and UO_3 correspondingly.

3.2. Density Functional Theory studies (DFT)

3.2.1. Geometry optimization

The completely optimized structure of the azo-azomethine **(H_2L, 1)** and its chelated complexes were shown in **Figure 4 and Figures S1-S3.** The chosen values for the lengths and angles of bond for complexes demonstrated a distorted octahedral or tetrahedral geometry around cations (Tables S1-S2). In complexes the azo-azomethine **(H_2L)** linked the metallic cations through the deprotonated/protonated phenolic oxygen and azomethine nitrogen atoms. They displayed a slight elongation at bond lengths of phenolic linkage (^{23}C-O^{25}) and a small shrinkage at bond lengths of the azomethine linkage (^{26}C-N^{27}). The bond length between the metallic cation and deprotonated phenolic oxygen atom was found to be in the range extended from 1.8100 to 2.2319 A°, while the bond lengths of protonated phenolic oxygen and azomethine nitrogen atoms were found to be in the range extended from 2.7003-3.1053 A°. In hexa-coordinated complexes Fe^{3+}, Co^{2+} and Zn^{2+} the four equatorial positions were occupied by phenolic oxygen, azomethine nitrogen, coordinated water oxygen and anion, while the two axial positions were occupied with two chelated water molecules, but in complexes **Ru^{3+}, VO^{2+}** and **Cu^{2+}(11)** the four equatorial positions were occupied by phenolic oxygen, azomethine nitrogen of the two ligand molecules, while the two axial positions were occupied with one chloride ion and one chelated water molecule as in **Ru^{3+}** complex or they were occupied with two chelated water molecules as in complexes **VO^{2+}** and **Cu^{2+}(11)**. In tetra-coordinated complexes **Ni^{2+}, Mn^{2+},** and **Cu^{2+} (8-10)** the four positions of tetrahedron were occupied by phenolic oxygen, azomethine nitrogen, coordinated water oxygen and anion. The bond angles in the coordination sphere of **Ru^{3+}, Fe^{3+}, VO^{2+}, Co^{2+}, Cu^{2+}(11),** and **Zn^{2+}** complexes were indicative to a distorted octahedral geometry, while the bond angles of Ni^{2+}, Mn^{2+}, and Cu^{2+} complexes **(8-10)** were indicative to a tetrahedral geometry.

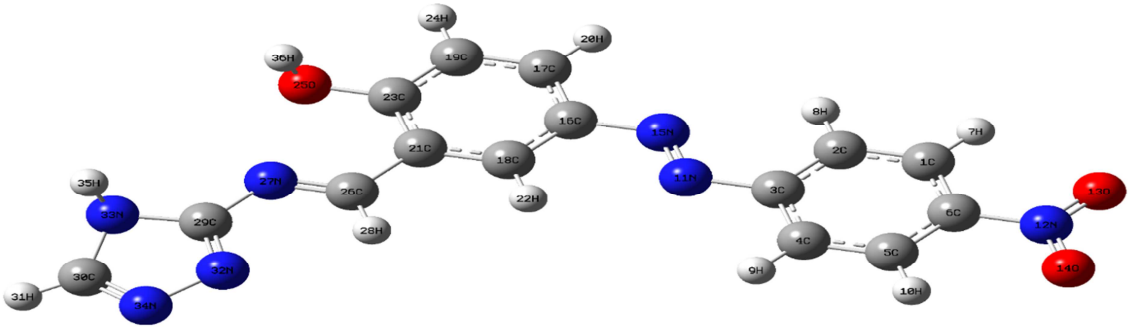

Figure 6. The Optimized structure for 2-((1H-1,2,4-triazol-5-yl)imino)methyl)-5-((4-nitrophenyl)diazenyl)phenol (H_2L, 1) by the DFT/B3LYP/6-311G(d,p)

3.2.2. Molecular parameters

Basing on Koopman theorem, The quantum chemical parameters of the azo-azomethine (H_2L, 1) and its metal chelates **(2-12)** were assessed and their data were itemized in **Tables 2-3** [73]. The molecular orbital of azo-azomethine and its chelated complexes (LUMO and HOMO) were illustrated by DFT/B3LYP/6-311G(d,p) calculation and it is presented in **Figure 7 and Figures S4-S6**. The positive and negative areas were illustrated using red and green colors consecutively. **Figure 7** showed that the LUMO molecular orbital was spread nearly over the azo moiety including the two phenyl rings and phenolic oxygen whereas the molecular orbital (HOMO) was spread over the azo linkage including some carbons of the phenyl rings as well as phenolic and azomethine nitrogen. The HOMO and LUMO energies as well as the energies of adjacent molecular orbitals are negative, indicating that the azo-azomethine molecule is stable [74]. The chelation of the azo-azomethine with metal cations happened via the phenolic oxygen atom (O-25), and azomethine nitrogen atom (N-27) which are the effective positions for chelation because of they have high electronegative charge.

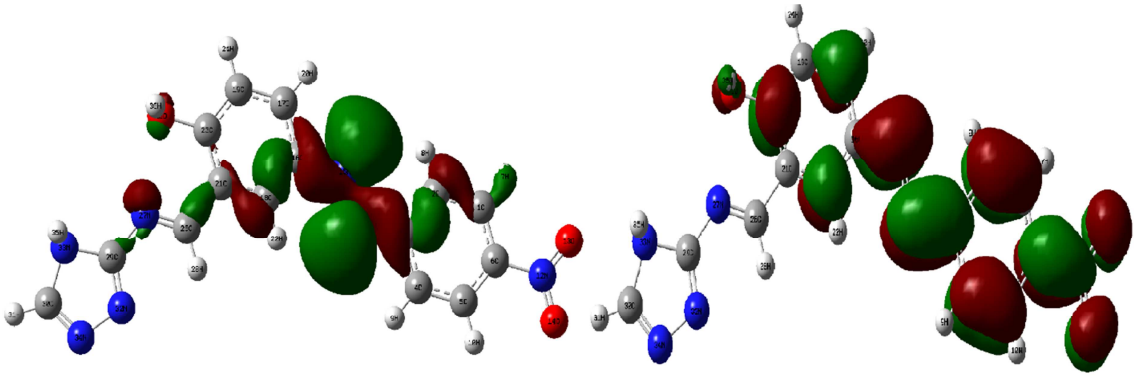

Figure 7. The 3D orbital pictures of the HUMO-LUMO level for azo-azomethine by the DFT/B3LYP/6-311G(d,p)

Table 2
The different quantum chemical parameters of ligand and its complexes (1-12)

No.	E_{HOMO} (eV)	IP	E_{LUMO} (eV)	EA	ΔE (eV)	χ (eV)	η (eV)	σ (eV^{-1})	Pi=-χ (eV)	ω (eV)	ΔN_{max}
HL	-0.3374	0.3374	-0.0132	0.0132	0.3242	0.1753	0.1621	6.17	-0.1753	0.0948	-1.08
(2)	-0.1828	0.1828	-0.1316	0.1316	0.0512	0.1572	0.0256	39.05	-0.1572	0.4827	-6.14
(3)	-0.2046	0.2046	-0.1264	0.1264	0.0782	0.1655	0.0391	25.57	-0.1655	0.3500	-4.23
(4)	-0.1404	0.1404	-0.0571	0.0571	0.0832	0.0987	0.0416	24.03	-0.0987	0.1171	-2.37
(5)	-0.2259	0.2259	-0.1019	0.1019	0.1240	0.1639	0.0620	16.13	-0.1634	0.2166	-2.64
(6)	-0.2019	0.2019	-0.1246	-0.155	0.0773	0.1632	0.0387	25.87	-0.1632	0.3446	-4.22
(7)	-0.1869	0.1869	-0.11668	0.1167	0.0703	0.1518	0.0351	28.47	-0.1518	0.3280	-4.32
(8)	-0.2289	0.2289	-0.12297	0.1230	0.1060	0.1760	0.0530	18.87	-0.1760	0.2922	-3.32
(9)	-0.2347	0.2347	-0.12741	0.1274	0.1073	0.1810	0.0536	18.65	-0.1810	0.3056	-3.38
(10)	-0.2326	0.2326	-0.12702	0.1270	0.1056	0.1798	0.0528	18.95	-0.1798	0.3063	-3.41
(11)	-0.1893	0.1893	-0.13345	0.1335	0.0559	0.1614	0.0279	35.78	-0.1614	0.4661	-5.78
(12)	-0.20815	0.2082	-0.13422	0.1342	0.0739	0.1712	0.0370	27.05	-0.1712	0.3964	-4.63

From **Figure 7** shows that the HOMO level is typically positioned on the phenolic oxygen (O-25) and azomethine nitrogen atom (N-27) indicating that the O-25 and N-27 atoms are the favored positions for nucleophilic attacking with the metallic cations inductive that these atoms have large coefficients of HOMO density and they are directed to the metal cations [75]. The values of separation energy (**$\Delta E=E_{LUMO}-E_{HOMO}$**) for the compounds **(1-12)** verified that the chelated complexes **(2-12)** are more reactive and less stable than the azo-azomethine **(H_2L, 1)** [76]. The energy lost if the system receives an extra electron is called electron affinity (**$EA=-E_{LUMO}$**) while The energy required to remove an electron from a species is known as the ionization potential (**$IP=-E_{HOMO}$**) [75, 77]. The absolute hardness (**$\eta=(IP-EA)/2$**) and absolute softness (**$\sigma=1/\eta$**) could be utilized as a scale to represent an atom's resistance to charge transfer and ability to receive electrons, respectively [78]. These two variables (**σ** and **η**) could be utilized to anticipate the stability and reactivity of molecules [78]. Soft molecules have a small energy gap, while hard molecules have a big energy gap. As a result, the reactivity of soft molecules is higher than that of hard molecules because soft molecules may easily transfer electrons to a receiver. In the coordinative compounds, the metal cations behave as a Lewis's acids while the ligand molecules behave as a Lewis's bases so, the ligand molecules are the most effective for coordination. The HOMO-LUMO which shows the reactivity of a molecule also describes the charge transfer possibilities in a molecule and its capability to transfer electron to an accepting specie. This feature (ease of electron to move from the HOMO to LUMO) is responsible for the bioactivity of the molecule. As seen in Figure 7 and Figure S9-11, the HOMO electron density is more distributed in the

backbone of complexes which also indicates higher reactivity [79]. Consequently, the chelator with an appropriate **σ** value has a well tendency to efficiently chelate the metallic cations. This conclusion is assured from the value of chelator's chemical potential (**Pi=-χ**) [74, 75]. From values of and reactivity index (ΔN_{max}**=−Pi/η**) absolute electronegativities (**χ=(IP+EA)/2**), chemical potentials (**Pi=-χ**), index of electrophilicity (**ω=Pi ^{2}/(2η)**), [80] we can conclude that: i) the reactivity index (N_{max}) is the measure of the system's energy stabilization when it gains an extra electronic charge from the surroundings. ii)The chemical potential (Pi) recognizes the quantity of charge and the direction in which it is transferred, where the electrophiles are the chemical that may take electrons from their surrounding and must reduce their energy when doing. So, its Pi values should be negative as reinforced by the data in **Table 2**. iii) The electrophilicity index (ω) determines a chemical species' ability to accept electrons. Therefore, the high ω value indicates a well electrophile while low value implies a well nucleophile. The ω values are low signifying to a well nucleophile. iv) The metallic cations were linked by azo-azomethine **(H_2L, 1)** *via* phenolic oxygen (O-25) and azomethine nitrogen atoms (N-27) which have high electronegative charge confirming that these atoms are the active sites for attachment. v) The complexes dipole moment values are ranged from 6.01 to 12.60 Debye which are greater than that of azo-azomethine, **(H_2L, 1)** (5.797 Debye), confirming that the attachment occurs *via* the phenolic oxygen (O-25) and azomethine nitrogen atoms (N-27). Other energetic properties of the synthesized compounds which are calculated by DFT method are listed in **Table 3.** The data in **Table 3** showed that the calculated binding energy of the complexes is more than that of azo-azomethine. This suggests that the chelated compounds is more stable than of the azo-azomethine [81].

3.2.3. Milliken atomic charges for the ligand

Milliken population analysis was used to determine the Milliken atomic charges of H_2L atoms by applying the DFT/B3LYP levels with the 6-311G(d,p) basis set in gas phase, and the results are shown in Figure S7 and listed in Table S3. The atomic charge playing a key role in the estimation of molecular system's quantum chemical parameters as the atomic charge effect on the vibrational spectra, electronic structure, polarizability, dipole moment, and other properties of molecular system [82]. The Milliken analysis data discovered that the hydrogen atoms have positive charge (1.112×10^{-1}-2.512×10^{-1} a.u), because of their losing electrons to the adjacent carbon atoms, whereas the hydrogen atoms attached to electronegative atoms (H-36 & H-35) have the highest positive charge of all hydrogen atoms due to their attachment to high electronegative atoms (O,N) [82]. All nitrogen and oxygen atoms except N-12 atom possess a negatively Milliken atomic charge demonstrating that these atoms acted as electron receptors and server as donating atom for chelating. The positive charge of N-12 may be due to its attachment to an electronegative atom (O-13&O-14).

Table 3
Some energetic properties of azo-azomethine and its complexes calculated by DFT method

No.	E_{HOMO} (*eV*)	E_{LUMO} (*eV*)	Total Energy (*eV*)	binding Energy (*a.u.*)	Dipole Moment (*Debye*)
HL	-0.3374	-0.0132	-0.3242	-1187.2	5.797
Ru^{3+}complex (2)	-0.1828	-0.1316	-0.0512	-3003	7.89
Fe^{3+}complex (3)	-0.2046	-0.1264	-0.0782	-3523.6	7.99
VO^{2+}complex (4)	0.1404-	-0.0571	-0.0833	3546	6.01
Co^{2+}complex (5)	-0.2259	-0.10189	-0.1240	-3026.9	12.35
Ni^{2+}complex (6)	-0.2019	-0.12457	-0.0773	-2999.8	10.26
Mn^{2+}complex (7)	-0.1869	-0.11668	-0.0703	-2642.4	12.41
Cu^{2+}complex (8)	-0.2289	-0.12297	-0.1060	-3363.8	11.15
Cu^{2+}complex (9)	-0.2347	-0.12741	-0.1073	-3183.9	11.51
Cu^{2+}complex (10)	-0.2326	-0.12702	-0.1056	-3132.0	12.60
Cu^{2+}complex (11)	-0.1893	-0.13345	-0.0559	-4865.0	12.22
Zn^{2+}complex (12)	-0.20815	-0.13422	-0.0739	-3423.4	10.89

3.2.4. Molecular electrostatic potential (MEP) and Electrostatic potential (ESP) analyses

To achieve the charge distributions and visualize variable for azo-azomethine (H_2L) molecule the ESP and MEP was estimated via DFT calculation

(**Figure 8**). MEP is a reactivity map that recognizes the positions of nucleophilic and electrophilic reactions on organic molecules, as well as hydrogen bonding interactions [82, 83]. MEP, V(r) at a certain position r(x, y, z) in the molecule's surrounding area, is recognized in terms of the energy interaction between the electric charge from the molecule's nuclei, electrons and proton situated at r. For the system examined the V(r) value was calculated by the following equation [82, 83].

$$\boldsymbol{V(r)} = \sum_{\boldsymbol{A}} \frac{\boldsymbol{Z_A}}{\boldsymbol{R_A - r}} \int \frac{\rho(\acute{r})}{(\acute{r} - r)} \boldsymbol{d}(\acute{r})$$

where, Z_A denoted to the charge of nucleus A, and is placed at R_A, $\rho(r')$ signifies to the electron charge density of molecule and r' indicates to the dummy integration variable [84]. The MEP used a variety of colors surface (from red to blue) to represent different electrostatic potential values on the molecule. The blue and red colors indicate the electropositive sites and electron-rich regions respectively while green color represented a region with electrostatic potential near zero. For anticipating the effective positions of nucleophilic and electrophilic attacks for azo-azomethine (**H_2L,1**) molecule**,** the 3D image of MEP and ESP utilizing the DFT/B3LYP/6-311G(d,p) method is shown in **Figure 6**. **Figure 6** shows that the highest positive potential places (blue) are centered on some carbon and hydrogen atoms, with values ranging from +0.11910-1 to 3.59310-1 a.u., indicating likely nucleophilic attack sites, However, the electronegative atoms (oxygen and nitrogen) have the highest negative potential, making them the preferred sites for chelation with metallic cations. These positions provide insight into the potential for intermolecular interactions. This result also suggests that hydrogen atoms are more attractive sites, whereas oxygen and nitrogen atoms are more repellent sites.

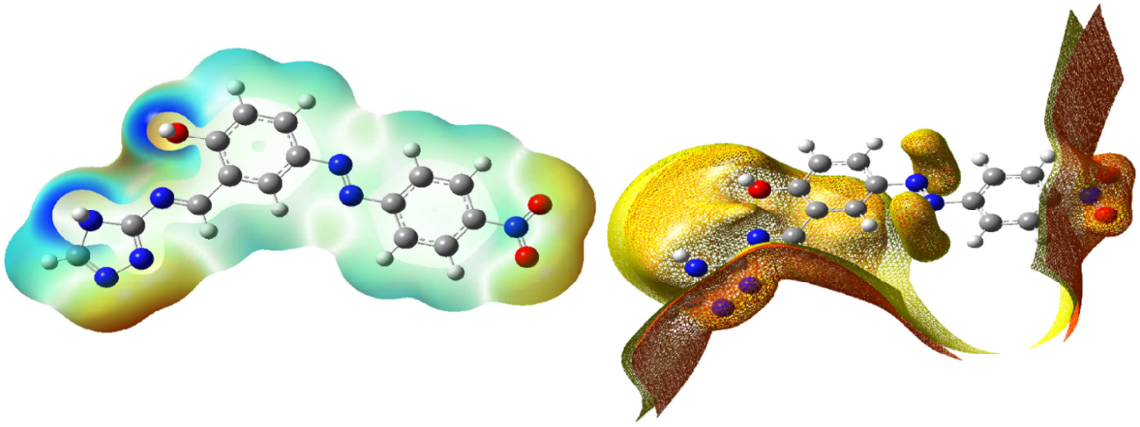

Figure 8: The 3d orbital images of Molecular electrostatic potential (MEP) and electrostatic potential (ESP) of the azo-azomethine (H_2L, 1) by DFT/B3LYP/6-311G(d,p)

3.3. Anti-microbial screening

The antimicrobial investigation results of the azo-azomethine (**H_2L,1**)**,** and its metal chelates **(2-13)** versus *B. subtilis, E. coli* (bacteria) and *A. niger* (fungus) is itemized in Table 4 and shown in **Figures 9-10**.

Table 4
The antimicrobial activity of prepared compounds (1 mg/mL/DMSO, at 28/37 °C, pH 7.4)

No	Inhibition zone (IZ, mm) and Activity Index (AI, %)					
	A. niger		*E. coli*		*B. subtilis*	
	IZ (mm)	AI (%)	IZ (mm)	AI (%)	IZ (mm))	AI (%)
DMSO	--	--	--	--	--	--
AmB	18	100%	--	--	--	--
Tc	--	--	34		33	
H_2L (1)	0	0%	0	0%	0	0%
Ru^{3+} complex (2)	9	50%	23	68%	25	76%
Fe^{3+} complex (3)	16	89%	19	56%	22	67%

VO^{2+} complex (4)	15	83%	21	62%	26	79%
Ni^{2+} complex (5)	14	78%	25	74%	22	67%
Co^{2+} complex (6)	14	78%	19	56%	20	61%
Mn^{2+} complex (7)	17	94%	22	65%	24	73%
Cu^{2+} complex (8)	10	56%	21	62%	15	45%
Cu^{2+} complex (9)	13	72%	23	68%	21	64%
Cu^{2+} complex (10)	15	83%	23	68%	25	76%
Cu^{2+} complex (11)	14	78%	25	74%	23	70%
Zn^{2+} complex (12)	17	94%	30	88%	28	85%
UO_2^{2+} complex (13)	13	72%	28	82%	22	67%

The complexes exhibited antifungal activity versus *A. niger* with inhibition zone ranged from 9 to 17 mm and activity indexes from 50% to 94%. Both of Mn^{2+} and Zn^{2+} complexes exhibited the same high potency of antifungal activity against *A. niger* with inhibition zone 17 mm and activity indexes 94% (of Am B). Ru^{3+}complex showed the least activity among all metal complexes investigated. The complexes exhibited antibacterial activity against *E. coli* and *B. subtilis* with inhibition zone ranged from 15 to 30 mm and activity indexes from 45% to 88%. The most potent complex against *E. coli* and *B. subtilis* is Zn^{2+} complex with inhibition zone 30 and 28 mm and activity index 88% and 85% respectively while the least potent complexes are **Fe^{3+}** and **Cu^{2+}(8)** complexes. In general, Zn^{2+} complex showed a unique potency in antifungal as well as antibacterial activities with very high potency close to Amphotericin B and tetracycline activities.

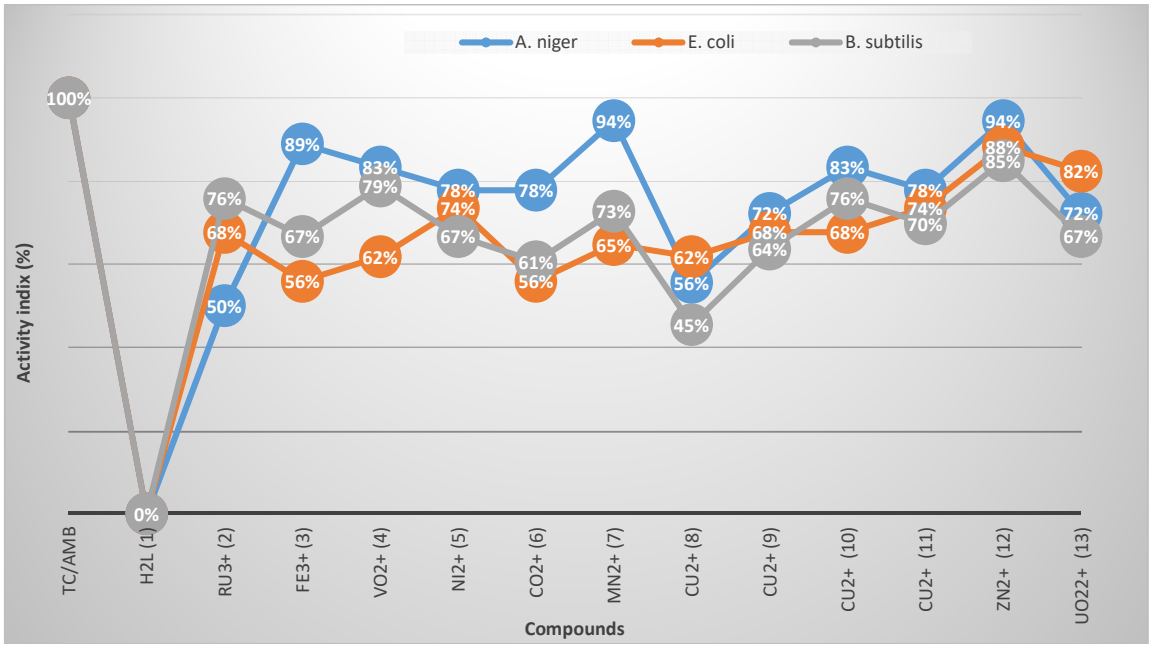

Figure 9: The activity index of antimicrobial activity of the azo-azomethine and its complexes (1 mg/mL/DMSO, at 28/37 °C, pH 7.4)

This finding makes it a promising complex which may be used as a new nucleus for antimicrobial drugs. This complex needs more study in the future. The complexes' antimicrobial action is higher than the azo-azomethine **(H_2L, 1)**. This can be clarified by the chelation theory.[94] According theory, the polarity of the metallic ions is weaken due to the partial sharing of the metallic ions charge with the chelator donor groups and the possibility of π-electron delocalization over the chelate rings. This weakens in the polarity leads to increase the lipophilic nature and assists in the permeation of the complex molecule into the microorganism lipid membrane [85, 86]. The high antifungal activity of some complexes may be attributed to the overlapping between the orbitals of metal and the molecular orbitals of ligand. The overlapping can contribute to additional distribution of the metallic positive charge with the donor group of ligand molecule. As a result, the polarity of the metallic ions is reduced leading to

an increase in the resonance of π-electrons and the lipo-solubility of the whole chelate. Therefore, it facilitates the diffusion of the metallic complex into microbes [85, 86]. The low activity of azo-azomethine and some of its metal complexes against some of the microbial strains might be attributed to the high polarity and hydrophobic nature of this compounds which decrease in the interaction with lipid membrane of the microorganism. Furthermore, these microbial strains' efflux pumps prevent these compounds from penetrating the lipid membrane, providing protection against these complexes [85, 86]. The high potency of zinc complexes may be attributed to the leaching of Zn^{2+} into the growth media, and its interference with the enzyme systems of the microbes.[87] In addition, the unique activity of zinc may be explained by the chelation theory which suggested the reason is the polarizability of the metal which can enhance the lipophilicity of the complexes [88]. In this study, some different cupper anions are used to prepare the metal complexes to study the effect of anion on the complexes activity which showed some changes in the activity according to the anion. In general chloride anion is more active followed by nitrate anion than the other anions for the same complex and this finding is coincided with a specific study on anion effect on antimicrobial activity of metal complexes [88].

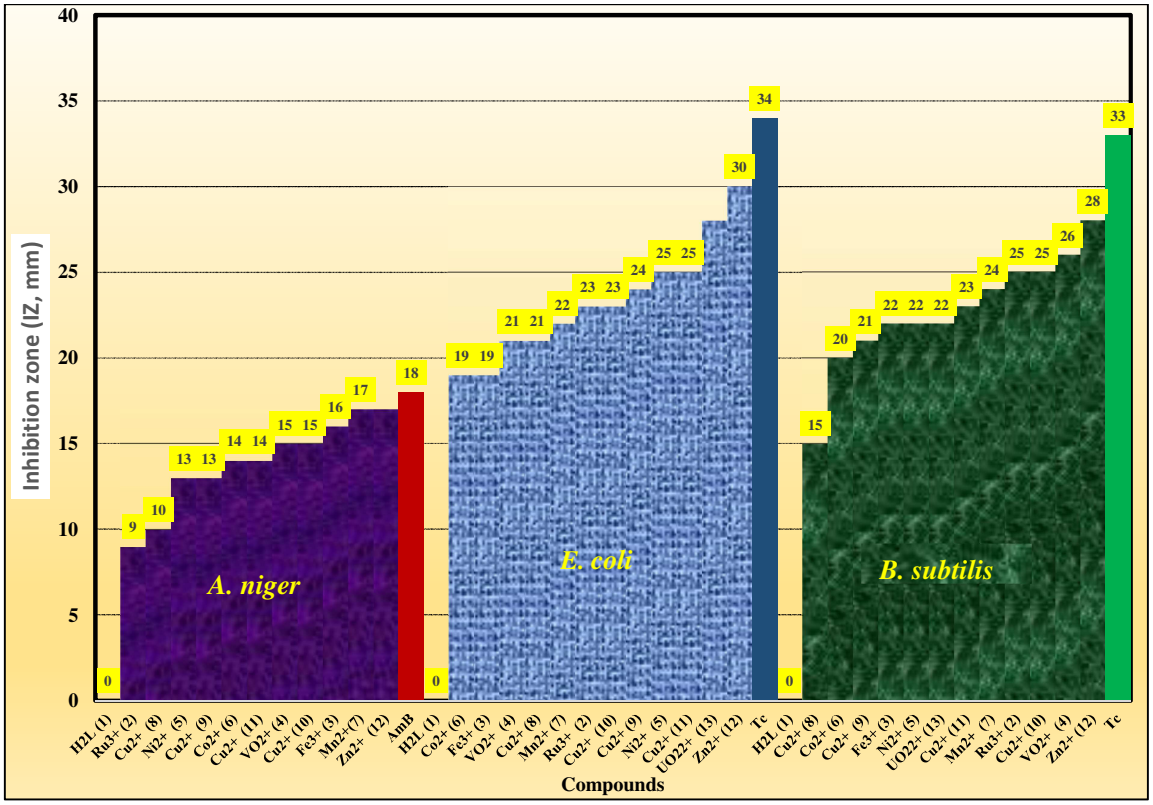

Figure 10: The Order of antimicrobial activity of azo-azomethine and its complexes (1 mg/mL/DMSO, at 28/37 °C, pH 7.4)

4. Conclusion

In this paper, azo-azomethine ligand namely, 2-((1H-1,2,4-triazol-5-yl)imino)methyl)-5-((4-nitrophenyl)diazenyl)phenol (H_2L, 1) and its Ru^{3+}, Fe^{3+}, VO^{2+}, Ni^{2+}, Co^{2+}, Mn^{2+}, Cu^{2}, Zn^{2+} and UO_2^{2+} have been synthesized and structurally characterized based on experimentally and theoretically tools. The results showed that the metal-chelator stoichiometry in all complexes is 1M:1L except Ru^{3+}, VO^{2+} and Cu^{2+}**(11)** complexes which was found to be 1M:2L. The azo-azomethine ligand functions as a monobasic/neutral bidentate chelator linking the metal centre through oxygen atom of deprotonated/protonated hydroxyl group and azomethine nitrogen atom adopting tetrahedral or distorted octahedral stereochemistry around metallic centre. All prepared compounds are stable because the energies of the HOMO and LUMO orbitals were small. The thermal analysis (TG) confirmed the formulae of studied complexes, where the thermo-decomposition took place in three or four stages ending with residue formed from metal oxide or metal oxide contaminated with carbon. The

antimicrobial data of the prepared compounds exhibited that the metal complexes, in general, possess a superior activity than the parent azo-azomethine. Among the newly prepared complexes is Zn^{2+} complex which showed the most active complex against fungal and bacterial strains. It showed activity resemble to amphotericin B and tetracycline. This finding provides a promising new model of compounds with high potency. In our future study, we will focus on creating novel hybrid metal complexes of azo-azomethine that may increase stability, may decrease the toxicity, and may enhance the biological activity, in addition, searching for new compounds is a valuable target to overcome the microbial resistance problems of antimicrobial agents.

5. Conflicts of interest

There are no conflicts to declare".

6. Funding Statement

This work was funded by the Deanship of Scientific Research (DSR), University of Jeddah, Jeddah, Saudi Arabia under grant no (UJ-02-063-DR). The authors, therefore, acknowledge with thanks the University of Jeddah for its technical and financial support.

7. Data Available statement

The data that supports the findings of this study are available in the supplementary material of this article.

8. References

[1] M.I. Abou-Dobara, M.A. Diab, A.Z. El-Sonbati, A.A. El-Bindary, A.M. Barakat, Correlation between the structure and biological activity studies of supramolecular coordination azodye compounds, Arab. J. Chem. 10 (2017) S1316-S1327.

[2] M.M.E. Shakdofa, A.A. Labib, N.A. Abdel-Hafez, H.A. Mousa, Synthesis and Characterization of VO^{2+}, Co^{2+}, Ni^{2+}, Cu^{2+} and Zn^{2+} Complexes of a Schiff base ligand derived from ethyl 2-amino-6-ethyl-4,5,6,7-tetrahydrothieno[2,3-c]pyridine-3-carboxylate and their Investigation as fungicide Agents, Appl. Organomet. Chem. 32(12) (2018) e4581.

[3] M. Sarigul, A. Sari, M. Kose, V. McKee, M. Elmastas, I. Demirtas, M. Kurtoglu, New bio-active azo-azomethine based Cu(II) complexes, Inorg. Chim. Acta 444 (2016) 166-175.

[4] M. Pervaiz, A. Riaz, A. Munir, Z. Saeed, S. Hussain, A. Rashid, U. Younas, A. Adnan, Synthesis and characterization of sulfonamide metal complexes as antimicrobial agents, J. Mol. Struct. 1202 (2020) 127284.

[5] R. Bentley, Different roads to discovery; Prontosil (hence sulfa drugs) and penicillin (hence β-lactams), J. Ind. Microb. Biotech. 36(6) (2009) 775-786.

[6] M. Pervaiz, S. Sadiq, A. Sadiq, U. Younas, A. Ashraf, Z. Saeed, M. Zuber, A. Adnan, Azo-Schiff base derivatives of transition metal complexes as antimicrobial agents, Coord. Chem. Rev. 447 (2021) 214128.

[7] T. Deb, D. Choudhury, P. S. Guin, M. B. Saha, G. Chakrabarti, S. Das, A complex of Co(II) with 2-hydroxyphenyl-azo-2′-naphthol (HPAN) is far less cytotoxic than the parent compound on A549-lung carcinoma and peripheral blood mononuclear cells: Reasons for reduction in cytotoxicity, Chemico-Bio. Inter. 189(3) (2011) 206-214.

[8] A. Mohammadi, B. Khalili, M. Tahavor, Novel push–pull heterocyclic azo disperse dyes containing piperazine moiety: Synthesis, spectral properties, antioxidant activity and dyeing performance on polyester fibers, Spectrochim. Acta Part A Mol. Biomol. Spectrosc. 150 (2015) 799-805.

[9] M. Tonelli, I. Vazzana, B. Tasso, V. Boido, F. Sparatore, M. Fermeglia, M.S. Paneni, P. Posocco, S. Pricl, P.L. Colla, C. Ibba, B. Secci, G. Collu, R. Loddo, Antiviral and cytotoxic activities of aminoarylazo compounds and aryltriazene derivatives, Bioorg. Med. Chem. 17(13) (2009) 4425-4440.

[10] P. Rani, V.K. Srivastava, A. Kumar, Synthesis and antiinflammatory activity of heterocyclic indole derivatives, Eur. J. Med. Chem. 39(5) (2004) 449-52.

[11] H. Xu, X. Zeng, Synthesis of diaryl-azo derivatives as potential antifungal agents, Bioorg. Med. Chem. Lett. 20(14) (2010) 4193-4195.

[12] A. Moanţă, S. Radu, Spectroscopic analysis and antimicrobial activity of some 4-phenylazo-phenoxyacetic acids, Rev. Roum. Chim. 54(2) (2009) 151-156.

[13] A. Pandey, R. Rajavel, S. Chandraker, D. Dash, Synthesis of Schiff Bases of 2-amino-5-aryl-1,3,4-thiadiazole and Its Analgesic, Anti-Inflammatory and Anti-Bacterial Activity, J. Chem. 9(4) (2012) 2524-2531.

[14] O.A. El-Gammal, F.S. Mohamed, G.N. Rezk, A.A. El-Bindary, Structural characterization and biological activity of a new metal complexes based of Schiff base, J. Mol. Liquids 330 (2021) 115522.

[15] M.A. El-Bindary, M.G. El-Desouky, A.A. El-Bindary, Metal–organic frameworks encapsulated

with an anticancer compound as drug delivery system: Synthesis, characterization, antioxidant, anticancer, antibacterial, and molecular docking investigation, Appl. Organomet. Chem. 36(5) (2022) e6660.
[16] M.A. El-Bindary, A.A. El-Bindary, Synthesis, characterization, DNA binding, and biological action of dimedone arylhydrazone chelates, Appl. Organomet. Chem. 36(4) (2022) e6576.
[17] M.H. Abdel-Rhman, R. Motawea, A. Belal, N.M. Hosny, Spectral, structural and cytotoxicity studies on the newly synthesized n'1,n'3-diisonicotinoylmalonohydrazide and some of its bivalent metal complexes, J. Mol. Struct. 1251 (2022) 131960.
[18] S.K. Sridhar, S.N. Pandeya, J.P. Stables, A. Ramesh, Anticonvulsant activity of hydrazones, Schiff and Mannich bases of isatin derivatives, Eur. J. Pharm. Sci. 16(3) (2002) 129-132.
[19] A.B. Thomas, R.K. Nanda, L.P. Kothapalli, S.C. Hamane, Synthesis and biological evaluation of Schiff's bases and 2-azetidinones of isonocotinyl hydrazone as potential antidepressant and nootropic agents, Arab. J. Chem. 9 (2016) S79-S90.
[20] M.A. Mahmoud, S.A. Zaitone, A.M. Ammar, S.A. Sallam, Synthesis, structure and antidiabetic activity of chromium(III) complexes of metformin Schiff-bases, J. Mol. Struct. 1108 (2016) 60-70.
[21] H.A. Kiwaan, A.S. El-Mowafy, A.A. El-Bindary, Synthesis, spectral characterization, DNA binding, catalytic and in vitro cytotoxicity of some metal complexes, J. Mol. Liquids 326 (2021) 115381.
[22] H.M.A. El-Lateef, M.M. Khalaf, M.R. Shehata, A.M. Abu-Dief, Fabrication, DFT Calculation, and Molecular Docking of Two Fe(III) Imine Chelates as Anti-COVID-19 and Pharmaceutical Drug Candidate, Int. J. Mol. Sci. 23(7) (2022).
[23] E.M. Conner, J. Reglinski, W.E. Smith, I.J. Zeitlin, Schiff base complexes of copper and zinc as potential anti-colitic compounds, Biometals 30(3) (2017) 423-439.
[24] R.E. Hester, E.M. Nour, Resonance Raman studies of transition metal peroxo complexes: 5—The oxygen carrier cobalt(II)-salen and its μ-peroxo complexes, [(L)(salen)Co]2O2; L = DMSO, py, DMF, pyO and no L, J. Raman Spectrosc. 11(2) (1981) 49-58.
[25] E. Jasim, E. Alasadi, R. Fayadh, M. Muhamman-Ali, Synthesis and Antibacterial Evaluation of Some Azo-Schiff Base Ligands and Estimation the Cadmium Metal by Complexation, Sys. Rev. Pharm. 11(6) (2020) 677 -687
[26] P. Pathak, V.S. Jolly, K.P. Sharma, Synthesis and Biological Activities of Some New Substituted Arylazo Schiff Bases, Orient. J. Chem. 16(1) (2017) 161-162.
[27] J.N. Liu, B.W. Wu, B. Zhang, Y. Liu, Synthesis and characterization of metal complexes of Cu(II), Ni(II), Zn(II), Co(II), Mn(II) and Cd(II) with tetradentate schiff bases, Turk. J. Chem. 30(1) (2006) 41-48.
[28] A.I. Vogel, Vogle's Text Book of Quantitative chemical Analysis, JOHN WIELY & SONS New York, 1989, p. 906.
[29] G. Svehla, Vogel's textbook of macro and semi micro Quantitative inorganic analysis, 5th ed., Longman Inc., New York, 1979.
[30] L. Lewis, R.G. Wilkins, Modern Coordination Chemistry, Interscience, New York, 1960.
[31] R.K. Boggess, D.A. Zatko, The use of conductivity data for the structure determination of metal complexes, J. Chem. Educ. 52(10) (1975) 649.
[32] M.J. Frisch, G.W. Trucks, H.B. Schlegel, G.E. Scuseria, M.A. Robb, J.R. Cheeseman, G. Scalmani, V. Barone, G.A. Petersson, H. Nakatsuji, X. Li, M. Caricato, A. Marenich, J. Bloino, B.G. Janesko, R. Gomperts, B. Mennucci, H.P. Hratchian, J.V. Ortiz, A.F. Izmaylov, J.L. Sonnenberg, D. Williams-Young, F. Ding, F. Lipparini, F. Egidi, J. Goings, B. Peng, A. Petrone, T. Henderson, D. Ranasinghe, V.G. Zakrzewski, N.R. J. Gao, G. Zheng, W. Liang, M. Hada, M. Ehara, K. Toyota, R. Fukuda, J. Hasegawa, M. Ishida, T. Nakajima, Y. Honda, O. Kitao, H. Nakai, T. Vreven, K. Throssell, J.A. Montgomery, Jr., J.E. Peralta, F. Ogliaro, M. Bearpark, J.J. Heyd, E. Brothers, K.N. Kudin, V.N. Staroverov, R. T. Keith, Kobayashi, J. Normand, K. Raghavachari, A. Rendell, J.C. Burant, S.S. Iyengar, J. Tomasi, M. Cossi, J.M. Millam, M. Klene, C. Adamo, R. Cammi, J.W. Ochterski, R.L. Martin, K. Morokuma, O. Farkas, J. B. Foresman, D.J. Fox, Gaussian 09, Revision A02, Gaussian, Inc, Wallingford CT,, 2016.
[33] T. Keith, J. Millam, GaussView, Version 5.0.9, Semichem. Inc.,, Mission, KS,, 2009.
[34] C. Lee, W. Yang, R.G. Parr, Development of the Colle-Salvetti correlation-energy formula into a functional of the electron density, Phys. Rev. B 37(2) (1988) 785-789.
[35] A.D. Becke, Density functional thermochemistry. III. The role of exact exchange, J. Chem. Phys. 98(7) (1993) 5648-5662.
[36] J. Collee, J. Duguid, A. Fraser, B. Marmion, Mackie and McCartney Practical Medical

Microbiology 5th edition Churchill Livingstone, Longman groups U. KLtd, 1989.

[37] I.A. Holder, S.T. Boyce, Agar well diffusion assay testing of bacterial susceptibility to various antimicrobials in concentrations non-toxic for human cells in culture, Burns 20(5) (1994) 426-429.

[38] W.J. Geary, The use of conductivity measurements in organic solvents for the characterisation of coordination compounds, Coord. Chem. Rev. 7(1) (1971) 81-122.

[39] J.F. Young, R.D. Gillard, G. Wilkinson, 992. Complexes of ruthenium, rhodium, iridium, and platinum with tin(II) chloride, J. Chem. Soc. (0) (1964) 5176-5189.

[40] H.G. Aslan, S. Özcan, N. Karacan, Synthesis, characterization and antimicrobial activity of salicylaldehyde benzenesulfonylhydrazone (Hsalbsmh)and its Nickel(II), Palladium(II), Platinum(II), Copper(II), Cobalt(II) complexes, Inorg. Chem. Commun. 14(9) (2011) 1550-1553.

[41] Z.H.A. El-Wahab, M.M. Mashaly, A.A. Salman, B.A. El-Shetary, A.A. Faheim, Co(II), Ce(III) and UO_2(VI) bis-salicylatothiosemicarbazide complexes: Binary and ternary complexes, thermal studies and antimicrobial activity, Spectrochim. Acta Part A: Mol. Biomol. Spectrosc. 60(12) (2004) 2861-2873.

[42] K. Nakamoto, Infrared and Raman Spectra of Inorganic and Coordination Compounds Part B: Applications in Coordination, Organometallic, and Bioinorganic Chemistry, 6th ed., John Wiley & Sons INC, USA, 2009.

[43] A.S. El-Tabl, M.M.E. Shakdofa, M.A. Whaba, Synthesis, characterization and fungicidal activity of binary and ternary metal(II) complexes derived from 4,4′-((4-nitro-1,2-phenylene) bis(azanylylidene))bis(3-(hydroxyimino)pentan-2-one), Spectrochim. Acta Part A: Mol. Biomol. Spectrosc. 136(PC) (2015) 1941-1949.

[44] C. Papatriantafyllopoulou, C.P. Raptopoulou, A. Terzis, J.F. Janssens, S.P. Perlepes, E. Manessi-Zoupa, Reactions of Nickel (II) Sulfate Hexahydrate with Methyl(2-pyridyl)ketone Oxime: Two Mononuclear Sulfato Complexes Containing the Neutral Ligand, Z. Naturforsch. B 62(9) (2007) 1123-1132.

[45] M.F.R. Fouda, M.M. Abd-Elzaher, M.M. Shakdofa, F.A. El-Saied, M.I. Ayad, A.S. El Tabl, Synthesis and characterization of a hydrazone ligand containing antipyrine and its transition metal complexes, J. Coord. Chem. 61(12) (2008) 1983-1996.

[46] M.M.E. Shakdofa, F.A. El-Saied, A.J. Rasras, A.N. Al-Hakimi, Transition metal complexes of a hydrazone–oxime ligand containing the isonicotinoyl moiety: Synthesis, characterization and microbicide activities, Appl. Organomet. Chem. 32(7) (2018) e4376.

[47] S.P. Dash, S. Pasayat, Saswati, H.R. Dash, S. Das, R.J. Butcher, R. Dinda, Oxovanadium(V) complexes incorporating tridentate aroylhydrazoneoximes: Synthesis, characterizations and antibacterial activity, Polyhedron 31(1) (2012) 524-529.

[48] Donald L. Pavia, Gary M. Lampman, George S. Kriz, J.R. Vyvyan, Introduction to Spectroscopy, 5th ed., Cengage Learning, USA, 2013.

[49] B.N. Bessy Raj, M.R.P. Kurup, N-2-Hydroxy-4-methoxyacetophenone-N′-4-nitrobenzoyl hydrazine: Synthesis and structural characterization, Spectrochim. Acta Part A: Mol. Biomol. Spectrosc. 66(4-5) (2007) 898-903.

[50] İ. Kaya, F. Kolcu, G. Demiral, H. Ergül, E. Kiliç, Synthesis and characterization of imine polymers of aromatic aldehydes with 4-amino-2-methylquinoline via oxidative polycondensation, Des. Monomers Polym. 18(1) (2015) 89-104.

[51] M.M.E. Shakdofa, N.A. Morsy, A.J. Rasras, A.N. Al-Hakimi, A.M.E. Shakdofa, Synthesis, characterization, and density functional theory studies of hydrazone–oxime ligand derived from 2,4,6-trichlorophenyl hydrazine and its metal complexes searching for new antimicrobial drugs, Appl. Organomet. Chem. 35(2) (2021) e6111.

[52] H.R. Fatondji, S. Kpoviessi, F. Gbaguidi, J. Bero, V. Hannaert, J. Quetin-Leclercq, J. Poupaert, M. Moudachirou, G.C. Accrombessi, Structure-activity relationship study of thiosemicarbazones on an African trypanosome: Trypanosoma brucei brucei, Med. Chem. Res. 22(5) (2013) 2151-2162.

[53] C.P. Pandhurnekar, E.M. Meshram, H.N. Chopde, R.J. Batra, Synthesis, Characterization, and Biological Activity of 4-(2-Hydroxy-5-(aryl-diazenyl)phenyl)-6-(aryl)pyrimidin-2-ols Derivatives, Org. Chem. Inter. 2013 (2013) 1-10.

[54] L.A. Baeva, L.F. Biktasheva, A.A. Fatykhov, N.K. Lyapina, Condensation of acetylacetone with formaldehyde and thiols, Russ. J. Org. Chem. 49(9) (2013) 1283-1286.

[55] Mohamad M. E. Shakdofa, A.S. El-tabl, A.S. Al-hakimi, M.A. Wahba, N. Morsy, Synthesis, structural characterization and microbicide activities of mononuclear transition metal complexes of 2-(2-hydroxy-5-(p-tolyldiazenyl) benzylidene) hydrazinecarbothioamide, Ponte 73(6) (2017) 52-74.

[56] T.K. Venkatachalam, G.K. Pierens, D.C. Reutens, Synthesis, NMR structural characterization and molecular modeling of substituted thiosemicarbazones and

semicarbazones using DFT calculations to prove the syn/anti isomer formation, Magn. Reson. Chem. 52(3) (2014) 98-105.
[57] N.M. Rageh, A.M.A. Mawgoud, H.M. Mostafa, Electronic spectra, solvatochromic behaviour, and acidity constants of some new azocoumarin derivatives, Chem. Pap. 53(2) (1999) 107-113.
[58] R. Gup, B. Kirkan, Synthesis and spectroscopic studies of copper(II) and nickel(II) complexes containing hydrazonic ligands and heterocyclic coligand, Spectrochim. Acta Part A: Mol. Biomol. Spectrosc. 62(4-5) (2005) 1188-1195.
[59] C. J. Ballhausen, Introduction to Ligand Field Theory, McGarw Hill, New York, USA, 1972.
[60] N.P. Priya, S. Arunachalam, A. Manimaran, D. Muthupriya, C. Jayabalakrishnan, Mononuclear Ru(III) Schiff base complexes: synthesis, spectral, redox, catalytic and biological activity studies, Spectrochim. Acta A Mol. Biomol. Spectrosc. 72(3) (2009) 670-6.
[61] M. Shebl, Mononuclear, homo- and hetero-binuclear complexes of 1-(5-(1-(2-aminophenylimino)ethyl)-2,4-dihydroxyphenyl)ethanone: Synthesis, magnetic, spectral, antimicrobial, antioxidant, and antitumor studies, J. Coord. Chem. 69(2) (2016) 199-214.
[62] S.L. Reddy, T. Endo, G.S. Reddy, Electronic (Absorption) Spectra of 3d Transition Metal Complexes, Advanced Aspects of Spectroscopy, InTech, United Kingdom, 2012.
[63] R. Sharma, S.K. Agarwal, S. Rawat, M. Nagar, Synthesis, Characterization and Antibacterial Activity of Some Transition Metal cis-3,7-dimethyl-2,6-octadiensemicarbazone Complexes, Transition Met. Chem. 31(2) (2006) 201-206.
[64] A.B.P. Lever, Inorganic electronic spectroscopy, Elsevier science, Amsterdam 1984.
[65] C. Anitha, C.D. Sheela, P. Tharmaraj, S. Johnson Raja, Synthesis and characterization of VO(II), Co(II), Ni(II), Cu(II) and Zn(II) complexes of chromone based azo-linked Schiff base ligand, Spectrochim. Acta Part A: Mol. Biomol. Spectrosc. 98 (2012) 35-42.
[66] Rajnikant, Synthesis and Studies on electronic spectra of Ni (II) Complexes with 3-hydroxy-2-Naphthalidene semicarbazone Int. J. Sci. Devel. Res. 5(3) (2000) 177-180.
[67] A.N.M.A. Alaghaz, H.A. Bayoumi, Y.A. Ammar, S.A. Aldhlmani, Synthesis, characterization, and antipathogenic studies of some transition metal complexes with N,O-chelating Schiff's base ligand incorporating azo and sulfonamide Moieties, J. Mol. Struct. 1035 (2013) 383-399.
[68] D.N. Sathyanarayana, Electronic Absorption Spectroscopy and Related Techniques, Universities Press2001.
[69] S. Chandra, S. Sharma, Synthesis and spectral studies of transition metal complexes with 1,5:11,15-dimetheno-2,4,10,12-tetramethyl-[1,5,9,13]-tetraazahexadeca-1,3,5,6, 10,11,13,15,16,20-decene a sixteen-membered tetradentate macrocyclic ligand, Transition Met. Chem. 32(2) (2007) 150-154.
[70] A.S. El-Tabl, M.M.E. Shakdofa, B.M. Herash, Antibacterial activities and spectroscopic characterization of synthetic metal complexes of 4-(3-(hydroxyimino)-4-oxopentan-2-ylidene)amino)-1,5- dimethyl-2-phenyl-1H-pyrazol-3(2H)-one, Main Group Chem. 12(3) (2013) 257-274.
[71] K.B. Gudasi, M.S. Patil, R.S. Vadavi, R.V. Shenoy, S.A. Patil, M. Nethaji, X-ray crystal structure of the N-(2-hydroxy-1-naphthalidene)phenylglycine schiff base. Synthesis and characterization of its transition metal complexes, Transition Met. Chem. 31(5) (2006) 580-585.
[72] R.-Ș. Mezey, I. Máthé, S. Shova, M.-N. Grecu, T. Roșu, Synthesis, characterization and antimicrobial activity of copper(II) complexes with hydrazone derived from 3-hydroxy-5-(hydroxymethyl)-2-methylpyridine-4-carbaldehyde, Polyhedron 102 (2015) 684-692.
[73] P. Geerlings, F. De Proft, W. Langenaeker, Conceptual Density Functional Theory, Chem. Rev. 103(5) (2003) 1793-1874.
[74] T.A. Yousef, O.K. Alduaij, G.M. Abu El-Reash, R.M. El Morshedy, Semiempirical studies, spectral analysis, in vitro antibacterial and DNA degradation studies of heterocyclic thiosemicarbazone ligand and its metal complexes, J. Mol. Liquids 222 (2016) 762-776.
[75] M.S. Masoud, A.E. Ali, M.A. Shaker, G.S. Elasala, Synthesis, computational, spectroscopic, thermal and antimicrobial activity studies on some metal–urate complexes, Spectrochim. Acta Part A Mol. Biomol. Spectrosc. 90 (2012) 93-108.
[76] N. Beyazit, B. Çatıkkaş, Ş. Bayraktar, C. Demetgül, Synthesis, characterization and catecholase-like activity of new Schiff base metal complexes derived from visnagin: Theoretical and experimental study, J. Mol. Struct. 1119 (2016) 124-132.
[77] J. B. Foresman, A. Frisch, Exploring Chemistry With Electronic Structure Methods: A Guide to Using Gaussian, , Gaussian, Pittsburgh, 1966.

[78] Z. Fakhar, T. Govender, G. Lamichhane, G.E.M. Maguire, H.G. Kruger, B. Honarparvar, Computational model for the acylation step of the β-lactam ring: Potential application for l,d-transpeptidase 2 in mycobacterium tuberculosis, J. Mol. Struct. 1128 (2017) 94-102.

[79] N.F. Ugwu, C.J.O. Anarado, C.U. Ibeji, O.C. Okpareke, C.J. Ezeorah, O.D. Okagu, A.C. Ekennia, F. Cömert, I. Babahan, B. Coban, O.T. Ujam, Synthesis, Spectroscopic, Antimicrobial Activity and Computational Studies of Some Homoleptic and Heteroleptic Metal(II) Complexes of 2-Furoic Acid Hydrazone, ChemistrySelect 4(37) (2019) 11206-11212.

[80] M. Sertçelik, Synthesis, spectroscopic properties, crystal structures, DFT studies, and the antibacterial and enzyme inhibitory properties of a complex of Co(II) 3,5-difluorobenzoate with 3-pyridinol, J. Chem. Res. 44 (2020).

[81] M.R. Mlahi, E.M. Afsah, A. Negm, M.M. Mostafa, Synthesis of 8-hydroxyquinolium chloroacetate and synthesis of complexes derived from 8-hydroxyquinoline, and characterization, density functional theory and biological studies, Appl. Organomet. Chem. 29(4) (2015) 200-208.

[82] A. Eşme, S.G. Sağdınç, Spectroscopic (FT–IR, FT–Raman, UV–Vis) analysis, conformational, HOMO-LUMO, NBO and NLO calculations on monomeric and dimeric structures of 4–pyridazinecarboxylic acid by HF and DFT methods, J. Mol. Struct. 1147 (2017) 322-334.

[83] P. Politzer, D.G. Truhlar, Chemical Applications of Atomic and Molecular Electrostatic Potentials:Reactivity, Structure, Scattering, and Energetics of Organic, Inorganic, and Biological Systems 1st ed., Springer, New York, 1981.

[84] P. Politzer, J.S. Murray, The fundamental nature and role of the electrostatic potential in atoms and molecules, Theor. Chem. Acc. 108(3) (2002) 134-142.

[85] M. Belicchi Ferrari, S. Capacchi, G. Pelosi, G. Reffo, P. Tarasconi, R. Albertini, S. Pinelli, P. Lunghi, Synthesis, structural characterization and biological activity of helicin thiosemicarbazone monohydrate and a copper(II) complex of salicylaldehyde thiosemicarbazone, Inorg. Chim. Acta 286(2) (1999) 134-141.

[86] R. Selwin Joseyphus, M. Sivasankaran Nair, Synthesis, characterization and biological studies of some Co(II), Ni(II) and Cu(II) complexes derived from indole-3-carboxaldehyde and glycylglycine as Schiff base ligand, Arab. J. Chem. 3(4) (2010) 195-204.

[87] S. Tavassoli Hojati, H. Alaghemand, F. Hamze, F. Ahmadian Babaki, R. Rajab-Nia, M.B. Rezvani, M. Kaviani, M. Atai, Antibacterial, physical and mechanical properties of flowable resin composites containing zinc oxide nanoparticles, Dent. Mater. 29(5) (2013) 495-505.

[88] O. Podunavac-Kuzmanović Sanja, D.C. Dragoljub, Anion effect on antimicrobial activity of metal complexes with benzimidazole derivative, Chem. Ind. Chem. Eng. Quart. 13(2) (2007) 68-71.